

**Author**

Forrest Gilfoxy

**Title**

Thermal State and Solidification Regime of the Martian Core:

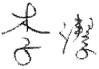
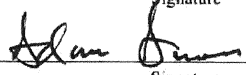

Insights from the Fe-Ni-S Liquidus at 20 GPa

submitted in partial fulfillment of the requirements for the degree of

**Master of Science in Earth and Environmental Sciences**

Department of Earth and Environmental Sciences

The University of Michigan

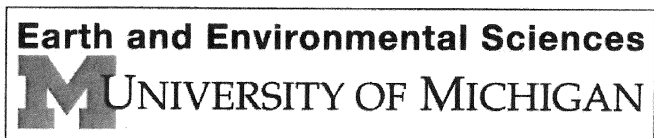
 Signature	Accepted by: <u>Jie Li</u> Name	<u>12/06/2016</u> Date
 Signature	<u>Adam Simon</u> Name	<u>12/07/2016</u> Date
 Department Chair Signature	<u>Chris J. Powlson</u> Name	<u>12/16/2016</u> Date

I hereby grant the University of Michigan, its heirs and assigns, the non-exclusive right to reproduce and distribute single copies of my thesis, in whole or in part, in any format. I represent and warrant to the University of Michigan that the thesis is an original work, does not infringe or violate any rights of others, and that I make these grants as the sole owner of the rights to my thesis. I understand that I will not receive royalties for any reproduction of this thesis.

- Permission granted.
- Permission granted to copy after: 07/01/2018
- Permission declined.

F.G.G

Author Signature



**© Copyrighted By**

Forrest Gilfoy

December 6, 2016

### **Acknowledgements**

Special thanks to my advisor, Professor Jackie Li, for her unwavering encouragement, advice in all subjects, and for her infectious passion for advancing the sciences. Thank you to Professor Adam Simon for his edits and helpful suggestions to this document. Thank you to Gordon Moore for his training and patience on the electron microprobe, and Will Bender for training on the SEM. Thanks to Heather Kirkpatrick, Jiachao (JC) Liu, Junjie (JJ) Dong, Zeyu Li, and Feng Zhu for help with my work and making the lab a place I didn't mind staying until midnight. Thanks you to the wonderful Earth department for fostering a healthy environment for education, research, and personal growth. Finally, thanks to all of my friends and family back home, especially my mom, dad, and sister, who may not have always understood what exactly I was spending my time doing the last few years, but supported me every step of the way.

**Author**

Forrest Gilfoy

**Title**

Thermal State and Solidification Regime of the Martian Core:

Insights from the Fe-Ni-S Liquidus at 20 GPa

submitted in partial fulfillment of the requirements for the degree of

**Master of Science in Earth and Environmental Sciences**

Department of Earth and Environmental Sciences

The University of Michigan

## Table of Contents

Acknowledgements.....	iii
List of Tables.....	vi
List of Figures.....	vii
Abstract.....	viii
Introduction.....	1
Methods.....	4
Results and Discussion.....	18
Conclusion.....	35
References.....	37
Supplemental Tables & Figures.....	47

## List of Tables

Table 1. Summary of Experimental Results.....	18
Table 2. Fitted Margules Parameters.....	26
Table 3. Parameters for Areotherm & Ideal Liquidus Curve.....	31
Supplementary Table. Target S Composition Vs. Estimate.....	47

## List of Figures

Figure 1. Power-Temperature Calibration.....	5
Figure 2. Optical Image of Run Product.....	7
Figure 3. BSE Image of Quenched Liquid, Fine Texture.....	8
Figure 4. BSE Image of Quenched Liquid, Limited Surface Area.....	9
Figure 5. Classification Process, Excluding Quenched Liquid Phase.....	11
Figure 6. Classification Process, Quenched Liquid Phase.....	12
Figure 7. Classification Results.....	14
Figure 8. EPMA Vs. Spatial Analysis.....	15
Figure 9. Subsolidus Phases.....	21
Figure 10. Margules, Ideal, & Liquidus Curves .....	25
Figure 11a. Concave Down Liquidii & 23 & 40 GPa.....	27
Figure 11b. Concave Up Liquidii & 23 & 40 GPa.....	28
Figure 12a. Areotherm Vs. Liquidii, Concave-down Construction.....	32
Figure 12b. Areotherm Vs. Liquidii, Parallel Construction.....	33
Supplemental Figure 1. Classification Assessment, Points.....	48
Supplemental Figure 2 Classification Assessment, Points.....	49

## Abstract

A series of multi-anvil experiments have been conducted to define the iron-rich liquidus of the iron-nickel-sulfur (Fe-Ni-S) system at 20 GPa, the estimated pressure of the Martian core-mantle boundary (CMB), across its entire temperature range. Due to the fineness of quenched liquid features at high temperatures and low S concentrations, spatial analysis techniques, in addition to electron microprobe analysis, were used to determine the compositions of some quenched liquid phases. The maximum concentration of S in the Fe(Ni) solid is only 0.6 wt.%, comparable to the Fe-S binary system, but far lower than prior results for the Fe-Ni-S system at 20 GPa. We attribute this to the tendency of FeNi alloys to form body-centered cubic (BCC) structures when at high Ni contents, in contrast with face-centered-cubic (FCC) structures when Ni contents are low. Our liquidus curve is nearly ideal, featuring a maximum temperature depression of 80 °C from 10 to 16 wt. % S, the likely range of Martian core composition. The slight negative departure from ideal behavior contrasts with the positive departure of liquidii previously applied to the Martian core without sufficient experimental constraints.

Unlike existing liquidii at 23 GPa, which predict a fully molten core for a narrow range of sulfur content between 14 and 15 wt. % S, our result is consistent with a molten state for all proposed core compositions, and establishes a new minimum CMB temperature of 1200 °C. Extrapolating our liquidus to high pressures and comparing it to calculated areotherms, we find that three core crystallization regimes are possible. For a Martian core with 10 to 12 wt. % S, crystallization takes the form of iron snow, while for cores with 13 to 16 wt. % S, solidification occurs near the center of the planet in the form of Fe<sub>3</sub>S crystallization. At 13 wt. % S, Fe<sub>3</sub>S would crystallize everywhere in the core, introducing a new scenario with uncertain and potentially interesting consequences for the Martian dynamo.

**Keywords:** Mars, core crystallization, iron snow, liquidus, Fe-Ni-S, high pressure, dynamo



## Introduction

Though the thermal state and composition of the Martian core has been studied for decades (Stevenson et al., 1983; Schubert & Spohn, 1990), results from the Mars Global Surveyor in 1997 uncovered a new layer of complexity on the subject – strong remnant magnetization of ~4 Ga impact basins in the planet's southern highlands (Acuna et al., 1999; Mitchell et al., 2001; Anderson et al., 1999). As planet-enveloping fields are generated by convection of conductive iron liquid in the core, the dearth of strongly magnetized rocks younger than 4 Ga in age is interpreted as evidence cataloging the death of an early Martian dynamo (Stevenson, 2001; Fassett & Head 2011). The initial dynamo was likely driven by thermal convection (Hauck & Phillips, 2002), due to the core being superheated relative to the mantle (Ke & Solomatov, 2009). Initial measurement of Mars's tidal Love number,  $k_2$ , and moment of inertia (MOI) suggested the Martian core is at least partially molten (Yoder et al., 2003).

As cores composed purely of Fe(Ni) would quickly crystallize (Stevenson et al. 1983), a non-solid Martian core indicates the presence of light elements capable of depressing the melting temperature. Density profiles consistent with Martian mantle and crustal mineralogy also require a significant presence of light elements in the core (Bertka & Fei, 1998, Fei & Bertka, 2005). The most common candidate is S, which has siderophilic tendencies and, as a volatile, is believed to be preferentially fractionated to Mars due to the planet's distance from the Sun (Sohl & Spohn, 1997). Though Khan & Connolly's (2008) thermal model allows for up to 25 wt. % S in the core, rheological, geochemical, & geodesic models place constraints of 10 – 16 wt. % S on the core S content (Wanke & Dreibus, 1988; Schubert & Spohn, 1990; Lodders & Fegley, 1997; Rivoldini et al., 2011).

While significant work has been devoted to understanding the cause of the dynamo's termination (Roberts & Arkani-Hamed, 2014; Hori & Wicht, 2013; Kuang et al. 2008) investigation of how a modern Martian dynamo might be regenerated has been limited to a single study. Based on Wanke & Dreibus's (1988) estimation of 74 wt. % Fe, 14.2 wt. % S, and 7.6 wt. % Ni for the Martian core, Stewart et al. (2007) performed multi-anvil melting experiments on the Fe-Ni-S system to determine its melting behavior at core conditions. By constraining Fe-Ni-S's eutectic temperature at the Martian CMB (23 GPa) and center (40 GPa), they interpolated liquidii slopes and compared them to the Martian core areotherm, which was assumed to have a gradient of  $25^{\circ}\text{C}/\text{GPa}$  (Williams & Nimmo, 2004; Fei & Bertka, 2005). The authors found that for a CMB temperature of  $1423^{\circ}\text{C}$ , (Hauck & Phillips, 2002), S contents of less than 14 wt. %, core crystallization would have already begun. More generally, they concluded that if the S content is on the Fe-rich side of the eutectic -16 wt. % S at 23 GPa - the two would cross at shallow depths causing Fe crystallization to initially occur near the CMB. If the composition is on the S-rich side, intersection would instead occur at Mars's center, producing solid  $\text{Fe}_3\text{S}$ .

The former core solidification scenario is colloquially referred to as the "iron snow" core crystallization regime due to its similarity to snowflakes crystallizing in the atmosphere and falling downward to accumulate on the ground. Iron crystallizes out of a sub-liquidus melt and falls inward under the force of gravity, dissolving into the liquid below before eventually precipitating at the center of the planet to form a solid inner core. While the iron snow crystallization regime has been confidently applied to small planetary bodies like Mercury (Chen et al. 2008; Dumberry & Rivoldini, 2015), Ganymede (Hauck et al. 2006), and our Moon (Jing et al. 2014), Mars's greater average core pressures render its mode of solidification ambiguous.

Work in the intervening years has helped to clarify the Martian core condition. Based on

mantle depletions of moderately siderophilic elements (Righter & Chabot, 2011; Chabot et al., 2011; Brandon et al., 2012) Rai & Van Westrenen (2013) posit the Martian core cannot exceed 10.6 wt. % S. Additional years of satellite data collection have led to improved estimates of the planet's (MOI) and tidal  $k_2$  Love number (Konopliv et al., 2011), indicating lower CMB pressures as well as a fully molten core. If the Martian CMB temperature is within the range discussed above, Stewart et al.'s liquidii are inconsistent with a fully molten core containing 10 wt. % S. While the Martian CMB is very difficult to constrain, there is also a high amount of uncertainty in the liquidus determinations, which are reliant upon a low number of data points. Mars's moderate size renders it amenable to being studied through high-pressure experimentation. Collectively, these new findings about the current state of the Martian core provide the impetus to re-evaluate the relationship between the Martian core areotherm and liquidii gradients.

To this end, we define the melting behavior of Fe-Ni-S at 20 GPa, the current estimate of the Martian CMB pressure (Rivoldini et al., 2011). 20 GPa is near the pressure that Fe<sub>3</sub>S stabilizes and undergoes a magnetic transition (Lin et al., 2004); as phase transitions have been linked to anomalous in the Fe-S system, our experiments will be necessary to avoid mischaracterizing the liquidus, and also to see how the Fe-Ni-S compares to its Fe-S counterpart at similar conditions. By defining the Fe-Ni-S liquidus along its entire Fe-rich domain, melting temperatures can be extrapolated to higher pressures with greater confidence. This melting data also provides a minimum estimate of the CMB temperatures. Finally, thermodynamic data will be used to calculate areotherms for the Martian core at the S end-members of 10 & 16 wt. % S. These areotherms and their relationship to the liquidii, will also determine which core crystallization regimes are possible within Mars.

## Methods

Melting experiments were performed using a Walker-type multi-anvil apparatus on the University of Michigan's campus in Ann Arbor, MI. To define the Fe-Ni-S liquidus across a range of temperatures, five unique starting materials were synthesized. The first two were produced by combining Fe (Alfa Aesar, 99.99% purity), Ni (Alfa Aesar, 99.99% purity) and S (Alfa Aesar, 99.99% purity) powders and grinding them under ethanol in an agate mortar to produce mixtures with the compositions of  $\text{Fe}_{82}\text{Ni}_8\text{S}_{10}$  and  $\text{Fe}_{91}\text{Ni}_8\text{S}_1$  (wt. %), respectively. The other three starting materials,  $\text{Fe}_{85}\text{Ni}_{10}\text{S}_5$ ,  $\text{Fe}_{88}\text{Ni}_{10}\text{S}_2$ , and  $\text{Fe}_{87}\text{Ni}_{10}\text{S}_3$ , were produced by a combination of Fe & Ni powders and un-ground  $\text{Fe}_{64}\text{S}_{36}$  grains (Alfa Aesar, 99.99% purity).

COMPRES's 8/3 cell assembly was used for all experiments (Leinenweber, 2012). Paper-backed Grade F tungsten carbide cubes, 3mm truncated edge length, compressed an 8mm edge length bored-out MgO octahedron, which housed the cell and serve as a pressure medium. Pyrophyllite gaskets were attached to the WC cubes parallel to the truncated edges so as to just touch the octahedron during final assembly. Fitted into a hole bored into the octahedra is a straight  $\text{LaCrO}_3$  furnace, enclosing a cylindrical resistance-heated Re sleeve. Centered in the sleeve is a cylindrical .98mm MgO capsule into which sample powder is packed to fill its middle third. For FeS grain experiments (see Results & Discussion) we individually placed ~.2 mm diameter grains in the .6 mm diameter capsule, positioning them in the middle of the Fe-Ni powder.

For experiments featuring a thermocouple (TC), the MgO capsule is book-ended on both sides by .25mm MgO disks. The top disk is followed by a .22mm  $\text{Al}_2\text{O}_3$  sliver, suspended above a 1.94mm bored-out  $\text{Al}_2\text{O}_3$  cylinder that carries type-C thermocouple ( $\text{W}_{95}\text{Re}_5$  and  $\text{W}_{84}\text{Re}_{16}$ ) leads towards the center of the assembly. The space between the termination of the TC leads and

the end of the plug is packed with Forsterite powder to stabilize it during compression. Above the  $\text{Al}_2\text{O}_3$  plug, the TC wires are secured by  $\text{Al}_2\text{O}_3$ -based cement and insulated by mullite sleeves. Below the bottom MgO disk, a 2.3mm  $\text{Al}_2\text{O}_3$  plug extends towards to the bottom of the Re heater. For non-TC experiments, the MgO capsule is followed on both ends by thicker 75mm MgO disks. Above and below these are .22mm  $\text{Al}_2\text{O}_3$  slivers, and finally by 2.1mm  $\text{Al}_2\text{O}_3$  plugs.

The run temperature of most experiments was estimated from a power vs. temperature calibration curve produced in our lab. This approach was adopted to maximize the chances of a successful run, as well as get a rough outline of the Fe-rich side of the liquidus, which was almost entirely unconstrained at the onset of our experiments.

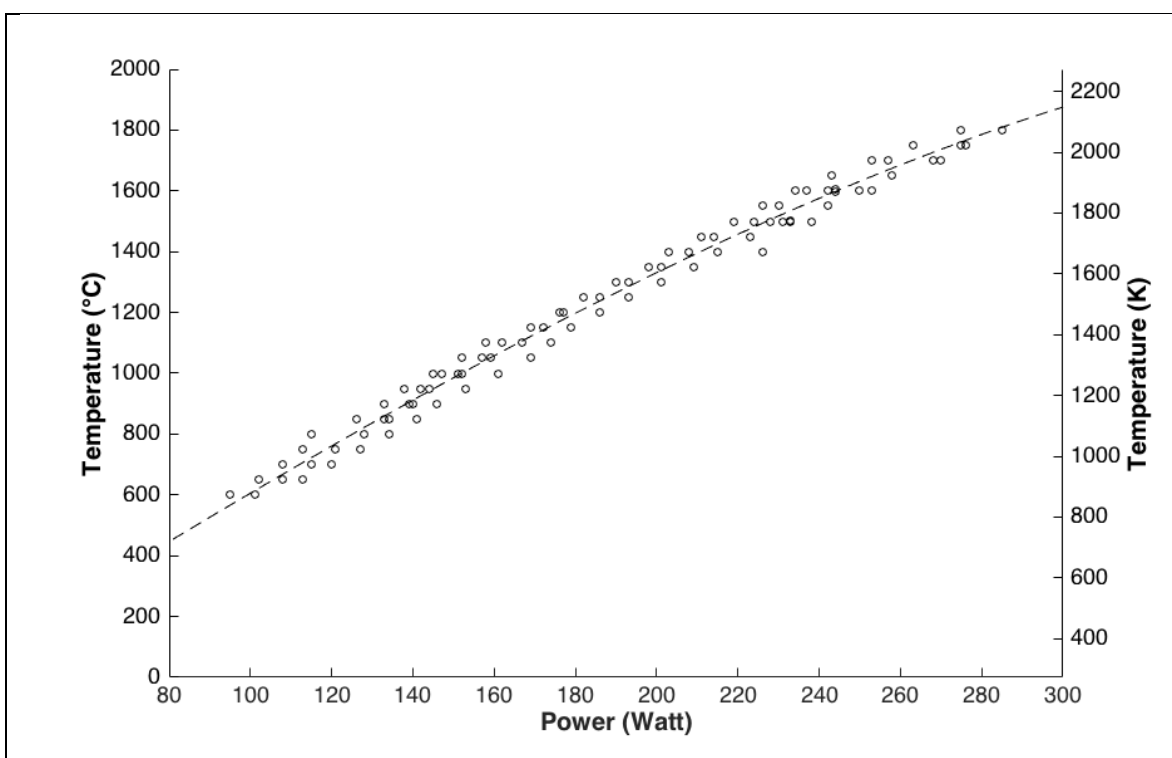


**Figure 1:** Power-temperature calibration based on data from four runs. Fit is least-squares polynomial,  $.00001x^3 - .0002x^2 + 8.3509x - 212.47$ ,  $R^2 = .987$ . The curve was then used to estimate the temperatures of non-TC experiments.

After the general shape of the liquidus had been determined, thermocouple runs were

conducted to provide tighter temperature constraints across the curve. With each TC run, the power-temperature calibration was updated in order to correct the temperature of the earlier runs, which relied upon an old calibration from our lab. Pressure was determined via a well-established calibration relationship between pressure experienced by the sample and the oil pressure of our multi-anvil, and was further constrained based on the stabilization of  $\text{Fe}(\text{Ni})_3\text{S}$  at 18 GPa (Pike et al., 1999).

Once loaded into the press, samples were brought to the target pressure of 20 GPa at a rate of 3.33 GPa/hr. Once pressures reached 5 GPa, sintering at 600 °C was initiated in order to lower the permeability of the MgO powder and prevent interaction between the sample and the Re heater. Upon reaching the target pressure of 20 GPa, each sample was heated at a rate of 100 °C per minute. For runs using Fe-Ni-S powder, the sample was heated directly to the target temperature after sintering. For runs featuring a mixture of FeS grains and powder, the sample was first heated to super-liquidus temperatures to ensure complete melting and homogenization of the sample, prior to being brought down to the target temperature. All samples were held at target temperatures for a minimum of 1 minute being rapidly quenched to room temperature by turning off the power. Decompression took 12 hours for a rate of ~1.66 GPa /Hr.

Following each run, we removed the octahedra from the multi-anvil and created a thick section by mounting the octahedron in epoxy. The mount was then ground on a wheel, parallel to the cylindrical heater, to expose the sample. During grinding, a Zeiss Stereo Microscope was used to take periodic images of the sample to determine the number and state of its phases. This process served as a precaution against inadvertently grinding through phases. Homogeneity and light color was interpreted as Fe(Ni)-rich solid phase, while a mixture of bright dendrites and dark interstitial liquid indicates a phase that was liquid prior to quenching (Fei et al., 2000).

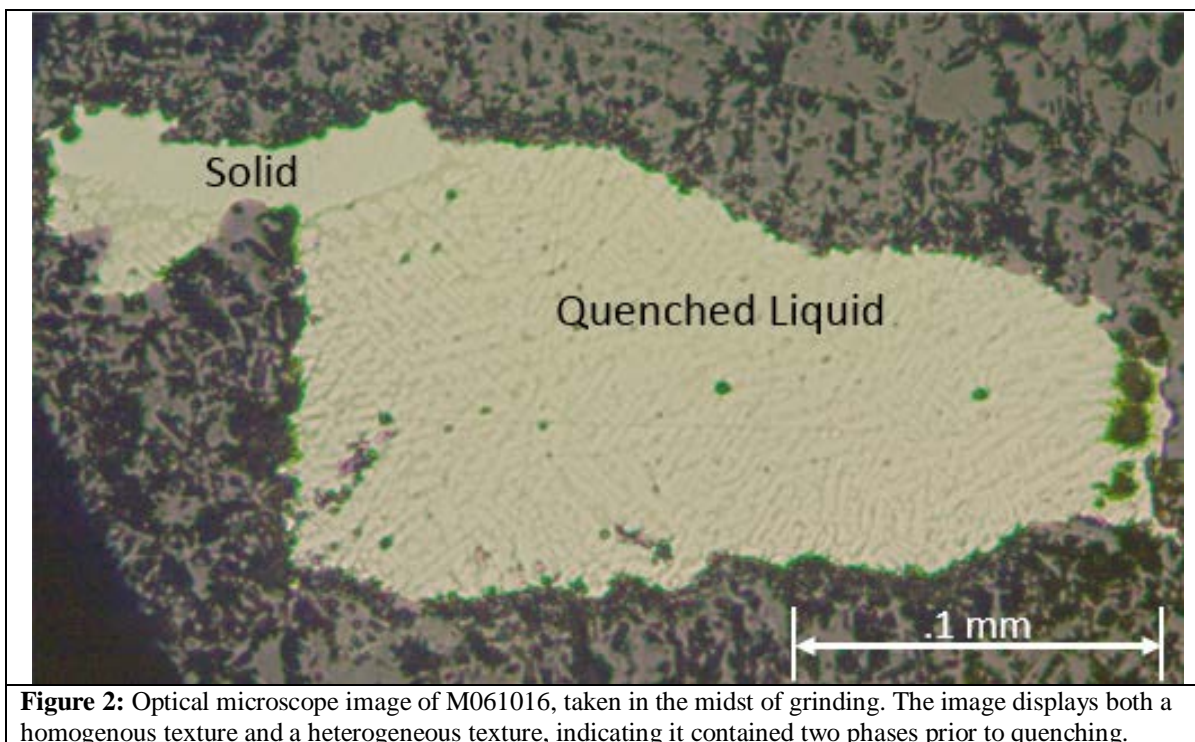


**Figure 2:** Optical microscope image of M061016, taken in the midst of grinding. The image displays both a homogenous texture and a heterogeneous texture, indicating it contained two phases prior to quenching.

To determine the chemical composition of the run products, the mounted and polished samples were carbon coated and a CAMECA SX-100 was used to conduct electron microprobe microanalysis (EPMA). Pyrite served as a dual standard for Fe and S, NiS was used for Ni, and MgCO<sub>3</sub> was used for Mg. Mg was included to indicate whether low measurements totals were the result of the beam straying onto the surrounding MgO matrix, or some other factor. Measurements that ranged beyond  $100 \pm 2$  wt. % total, as well as those with more than .1 wt. % Mg were discarded. Beam conditions of 15 keV, 15 nA, and 30 second counting times with 15 s backgrounds were applied to Fe, Ni & S. For Mg, a shorter 10 s counting time was used.

Two beam sizes were employed: a "0"  $\mu\text{m}$  point beam and a  $5\mu\text{m}$  de-focused beam. For the homogenous solid (Fig. 2, top left), the point beam and  $5\mu\text{m}$  beam gave indistinguishable results and were subsequently used interchangeably. The composition of the alloy phase was taken as the average of all measurements, with the uncertainty given as the standard error. For the quenched liquid phase (Fig. 2, right) multiple measurements with the  $5\mu\text{m}$  beam, spanning

the sample surface, were taken and subsequently averaged. While this defocused beam analysis approach (DBA) was effective for most run product analysis, difficulties arose in sulfur-poor samples where the liquid phase became heterogeneous, at small scales, upon quenching. The uneven distribution of Fe(Ni)-rich dendrites and S-rich liquid introduced a large amount of variability in our  $5\mu\text{m}$  measurements.

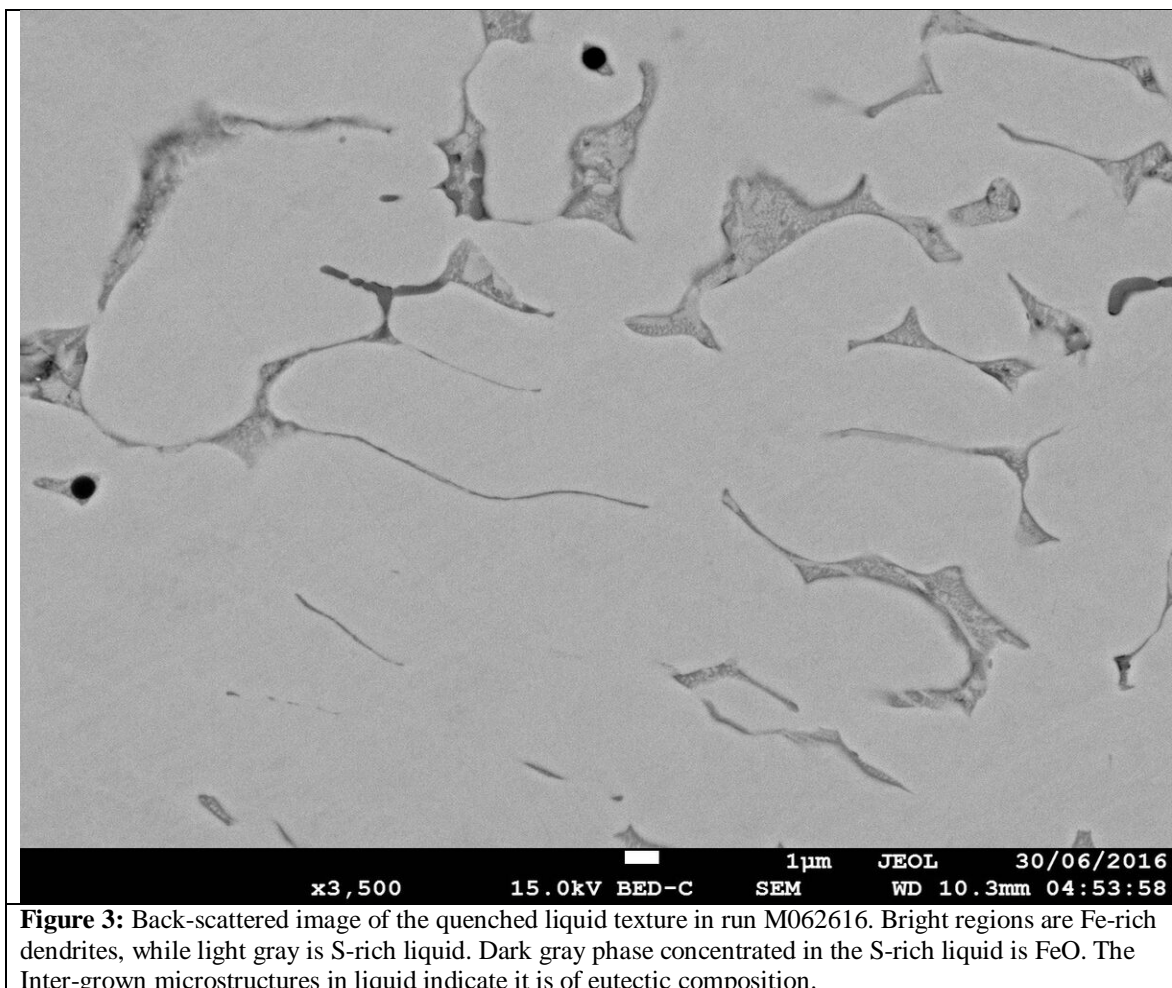


**Figure 3:** Back-scattered image of the quenched liquid texture in run M062616. Bright regions are Fe-rich dendrites, while light gray is S-rich liquid. Dark gray phase concentrated in the S-rich liquid is FeO. The Inter-grown microstructures in liquid indicate it is of eutectic composition.

In these cases, a point beam was instead rastered across  $10 \times 10 \mu\text{m}$  areas of sample, covering both dendrite and interstitial liquid textures. We tested the raster method versus DBA method and found results differed by less than 1 wt. %, leading us to conclude that the two methods are directly comparable, and we used them interchangeably to create our data set. However, for some very S-poor runs, both the DBA and raster approach resulted in quenched



liquid compositions that were too depleted in S to be credible. Due to the fineness of the S-rich interstitial liquid in relation to the Fe-rich dendrites, it is likely that the beam inadvertently excited electrons in the adjacent dendrite, producing secondary fluorescence that increased Fe count totals. While lowering the beam voltage has been explored as a solution, this requires the sampling soft X-rays (Gopon et al., 2012), which have poorly constrained mass attenuation coefficients and are prone to peak shifts and C contamination due to their relatively low count rate (Merlet & Llovet, 2012). In other samples, only a very small area of quenched liquid phase was available for analysis. As a result, the number of 5  $\mu\text{m}$  measurements was small, and 10 x 10  $\mu\text{m}$  rasters tended to stray onto the solid or MgO matrix, and uncertainty in the data was large.

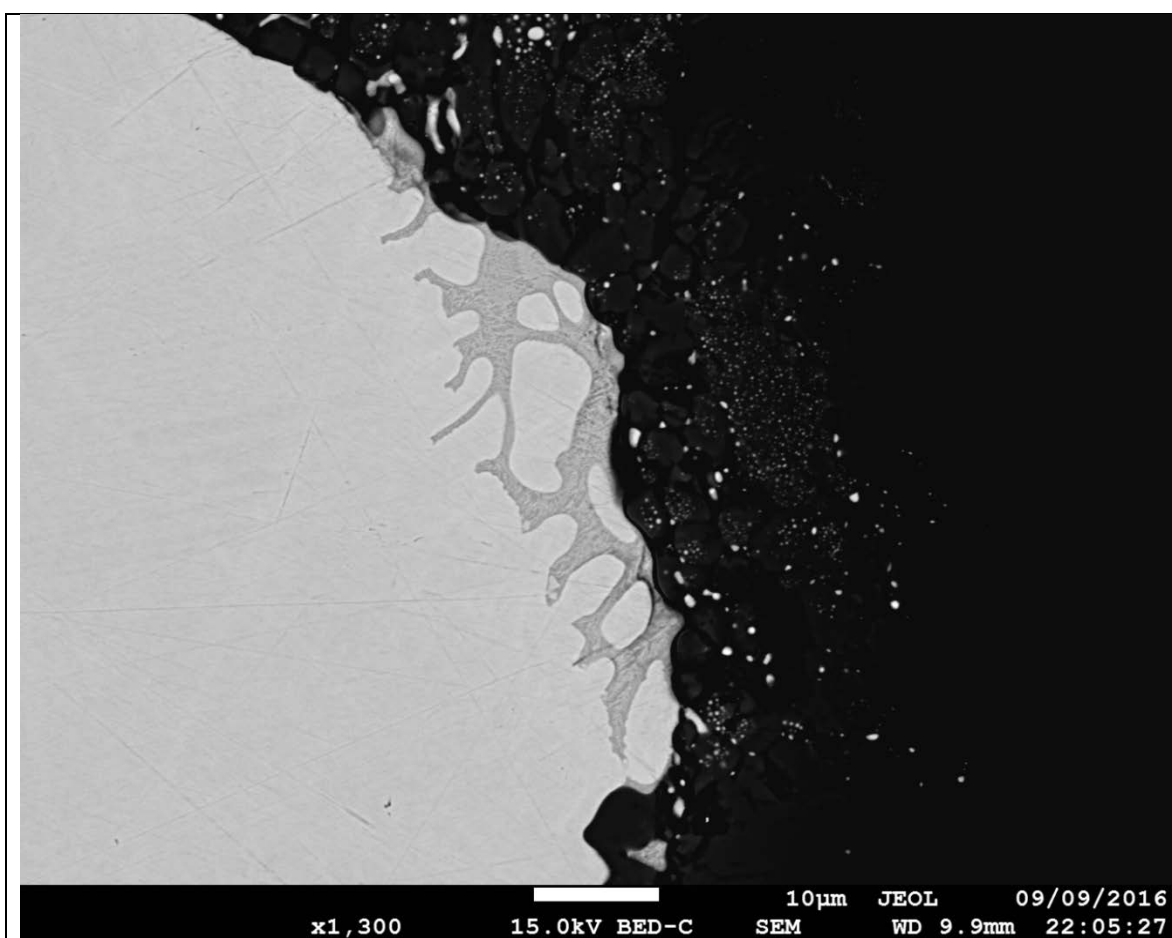


**Figure 4:** Quenched liquid region of run M062016. Note limited surface area, specified in scale bar at bottom, when compared to 5  $\mu\text{m}$  defocused beam, and 10  $\mu\text{m}$  length area needed for raster analysis. This run will hereafter be used to explain the spatial analysis process.

Following the work of others (Grande, 2000) we decided to estimate the composition of the quenched liquid phase by performing image analysis on the sample. This process was motivated by the principle that if the surface area of each phase could be accurately determined, the composition of the sample could then be estimated by multiplying each phase's areal fraction by that phase's individual chemical composition. Geographical Information Software (GIS) was used to perform the analysis, which we term "spatial analysis" due to the fact that we rely upon EPMA for discrete chemical information, and the image analysis for the spatial extent of phases. Though typically reserved for mapping features at the macroscopic scale, the program has been recently applied to the identification of grain boundaries in thin sections (Li et al., 2008). We began by converting back-scattered (BSE) images of the samples into a high-resolution raster. As BSE image brightness corresponds directly to the chemical composition of the object sampled, we used color as a metric to dis-aggregate our sample into solid, liquid, and dendrite phases.

This process of data segmentation was accomplished by using GIS's image classification tool to organize the raster's cells into classes based on their color and distance to like-colored cells. While GIS offers unsupervised analysis, in which the program automatically chooses classes by prioritizing certain colors, we found that supervised analysis, in which the user manually identifies color regions, is a more accurate way to map the sample. GIS's Training Sample Manager was used to select regions on the raster, visible as crosshatched polygons in Figs. 5 & 6, that serve as a guide to classify each cell into a group. Three of these, the gray, S-rich liquid (dark green), the bright Fe-rich dendrite (orange), and the bright solid (purple), are present within the sample, and are subsequently used to determine its chemical composition. The other two textures (the red and light green) are representative of disconnected droplets of sample and holes in the sample and are selected for the purpose of filtering them out from subsequent

analysis. Using these categorizations as a guide, cluster analysis was then performed on the sample to separate it into the classes enumerated above.

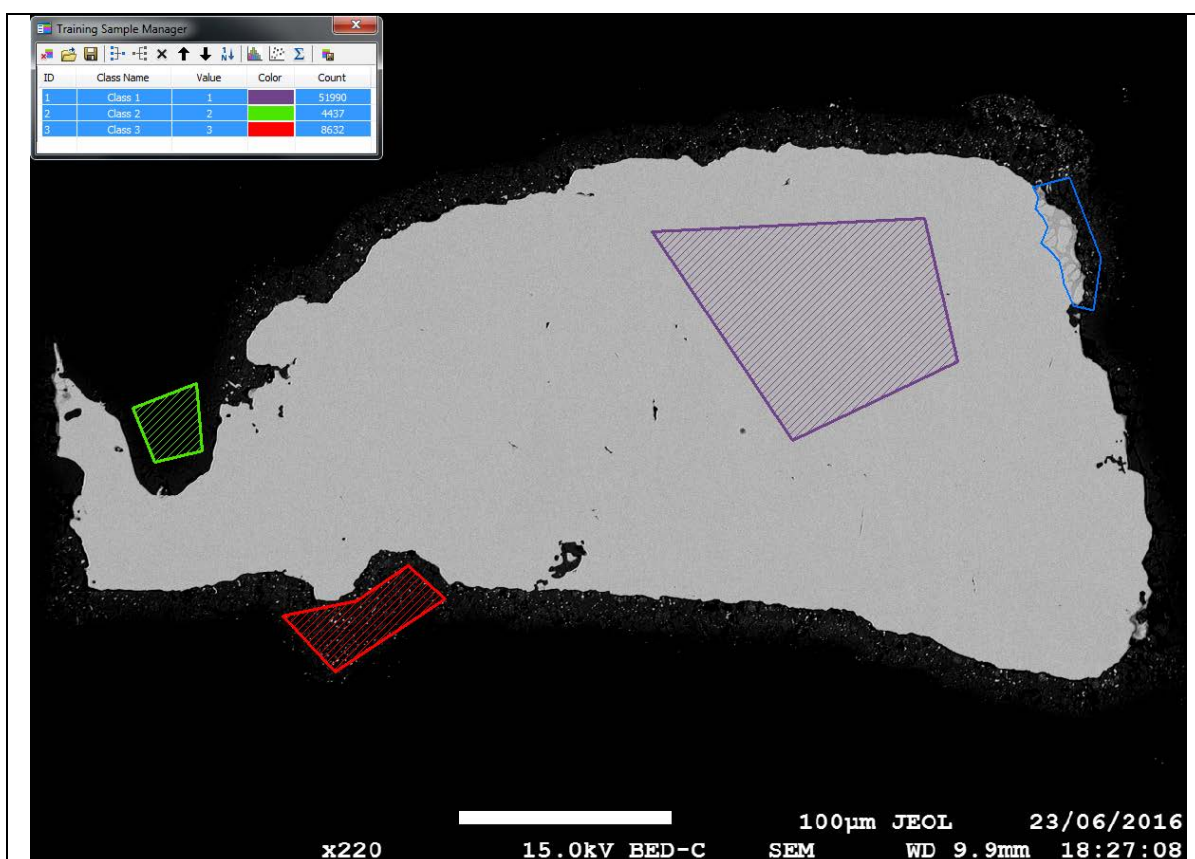


**Figure 5:** Screenshot of the classification process in GIS as applied to determining the amount of solid in run M062016. The quenched liquid phase is outlined by blue polygon in upper right. This polygon served as a mask, preventing the enclosed area from participating in image classification so that the area of the solid phase could be determined in isolation. Class 1, in purple, represents the solid, homogeneous, Fe(Ni) solid. Class 2, in red, contains droplets of sample in the MgO matrix and is meant to exclude this texture from counting as a sample. Class 3, corresponds to the MgO matrix, including sample holes, and is meant to exclude these textures from analysis. While finding the area of the solid is not critical to determining the composition of the quenched liquid phase, it was undertaken to estimate the bulk composition of all samples.

Due to the near-identical brightness of the Fe-rich solid and the Fe-rich dendrites in the quenched liquid phase, an extra step was taken in analysis of all two-phase samples to avoid combining the two textures within the same class. To this end, a polygon (shown in blue, Fig. 5) was manually drawn around the quenched liquid phase to isolate it from the solid phase. From here, analysis was constrained to the area of raster within polygon (the quenched liquid phase),

or without it (the solid phase), by means of a GIS's “mask” feature, which limits the extent to of cluster analysis. For most samples, only a single, full-sized BSE image was needed to perform this analysis, however the smallness of the quenched liquid in Fig. 4 results in the resolution being insufficient to provide an accurate estimation of the liquid and dendrite areas. Therefore, this region was analyzed at higher magnification, visible in Fig. 6, in the same manner as described in Fig. 5, save that cluster analysis is restricted to the area within the mask rather than without.

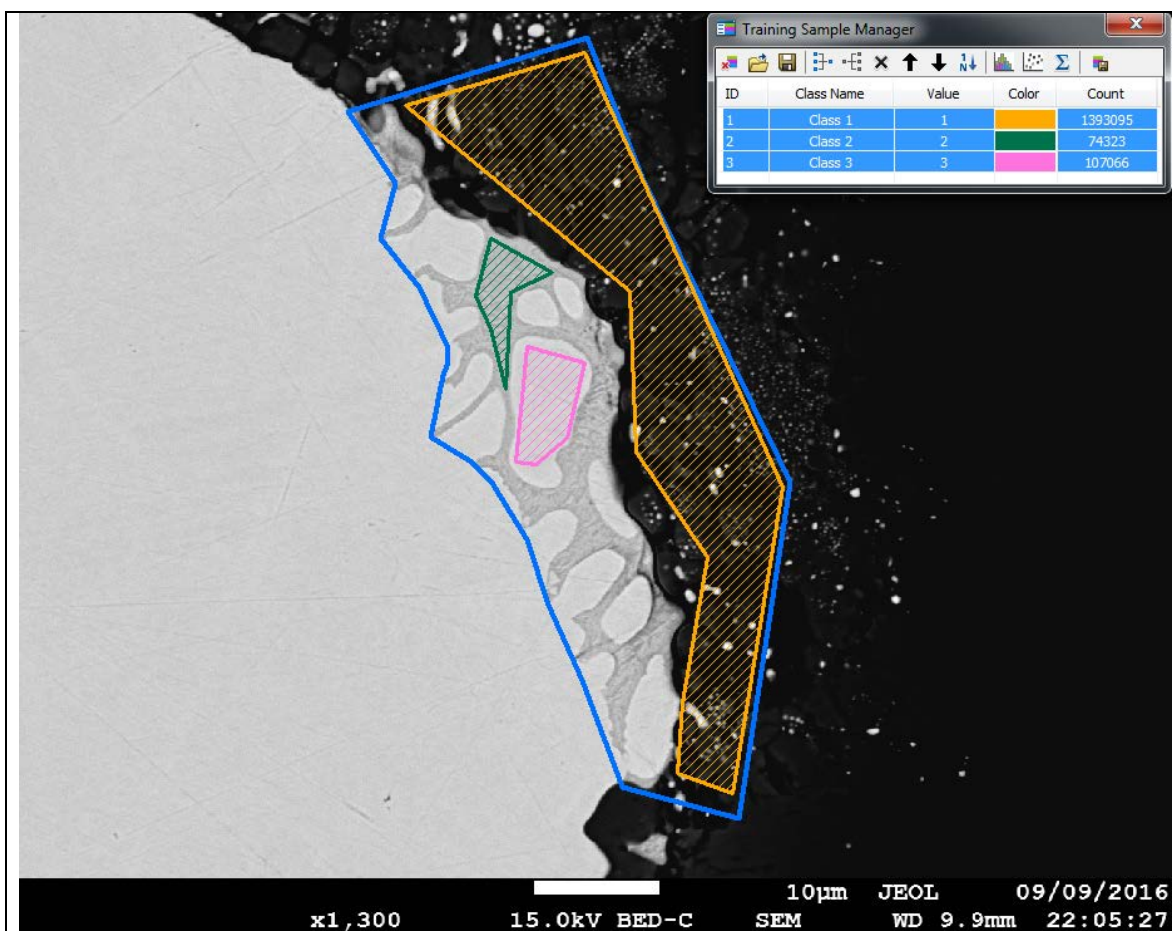


**Figure 6:** Screenshot of the categorization process in GIS as applied to run M062016. As in Fig. 5, blue polygon limits the extent of analysis, in this case restricting it to within polygon's borders to isolate the quenched liquid phase. The three cross-hatched polygons correspond to distinct compositions: Class 1, in orange, contains droplets of sample in the MgO matrix and is meant to exclude this texture from counting as a sample. Class 2, in green, is the S-rich liquid. Class 3, pink, corresponds to the Fe-rich dendrite.

The areal fraction of liquid and dendrite is determined by dividing their individual areas

by their combined total. As can be seen in Fig. 6, some of these droplets are included in the dendrite, solid, or liquid classes, providing proof that the image classification process is not perfect. Uncertainties associated with the classification process were estimated by evaluating how well the resulting classified image matched the original. The accuracy of classifying a particular phase is the sum of the number of training cells correctly classified as that phase, divided by the total number of training cells that should have been classified as the phase based on our initial assessment (see Suppl. Figs. 1 & 2). All fractional accuracy values were above .9, indicating the classification process was effective at reproducing the original image.

When possible, a point beam was used to determine the composition of the S-rich liquid and dendrite. However, for S-poor experiments the area of the liquid was often too small to get an accurate measurement, while for S-rich experiments the same was true of the dendrite. In these cases, we assigned the dendrite a composition of  $89.9 \pm .1$  wt. % Fe,  $8.69 \pm .02$  Ni, and  $0.58 \pm .02$  wt. % S, the measurement of the highest S concentration in the solid of any run in our dataset. The liquid was likewise assigned a value of  $75.36 \pm .09$  wt. % Fe,  $9.57 \pm .16$  wt. % Ni, and  $15.84 \pm .05$  wt. % S, Zhang & Fei's (2008) sub-solidus result at  $\sim 10$  wt. % Ni. While it is not our data point, this value is reasonable given the system's proximity to the stabilization of  $\text{Fe}_3\text{S}$  &  $\text{Fe}(\text{Ni})_3\text{S}$  (Fei et al., 2000; Pike et al., 1999). Uncertainties for the quenched liquid phase are the combined errors of the liquid and dendrite values, multiplied by the inverse of the classification accuracy of the given run.

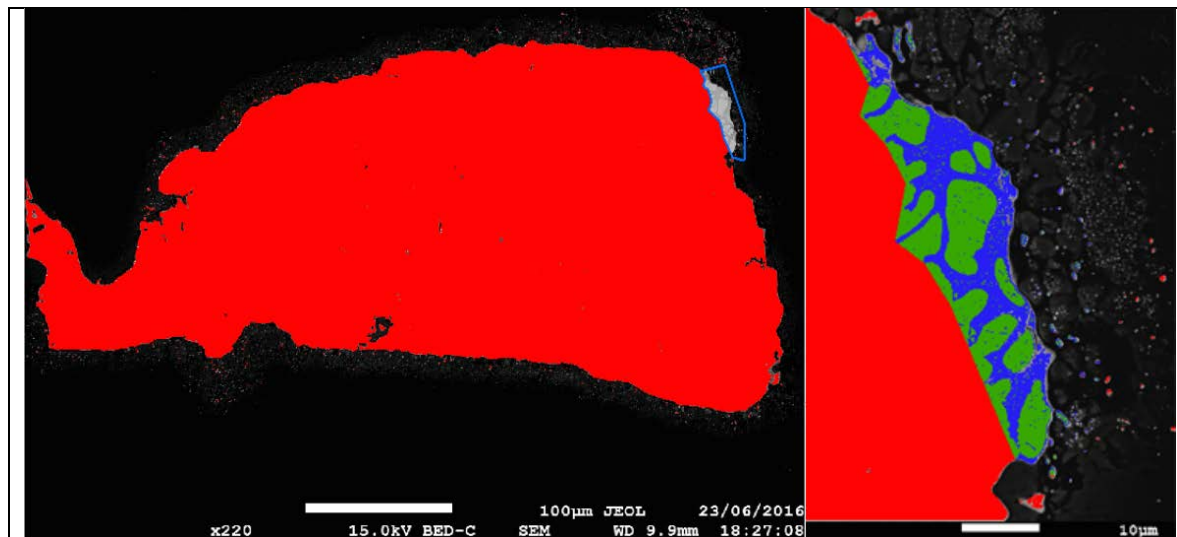
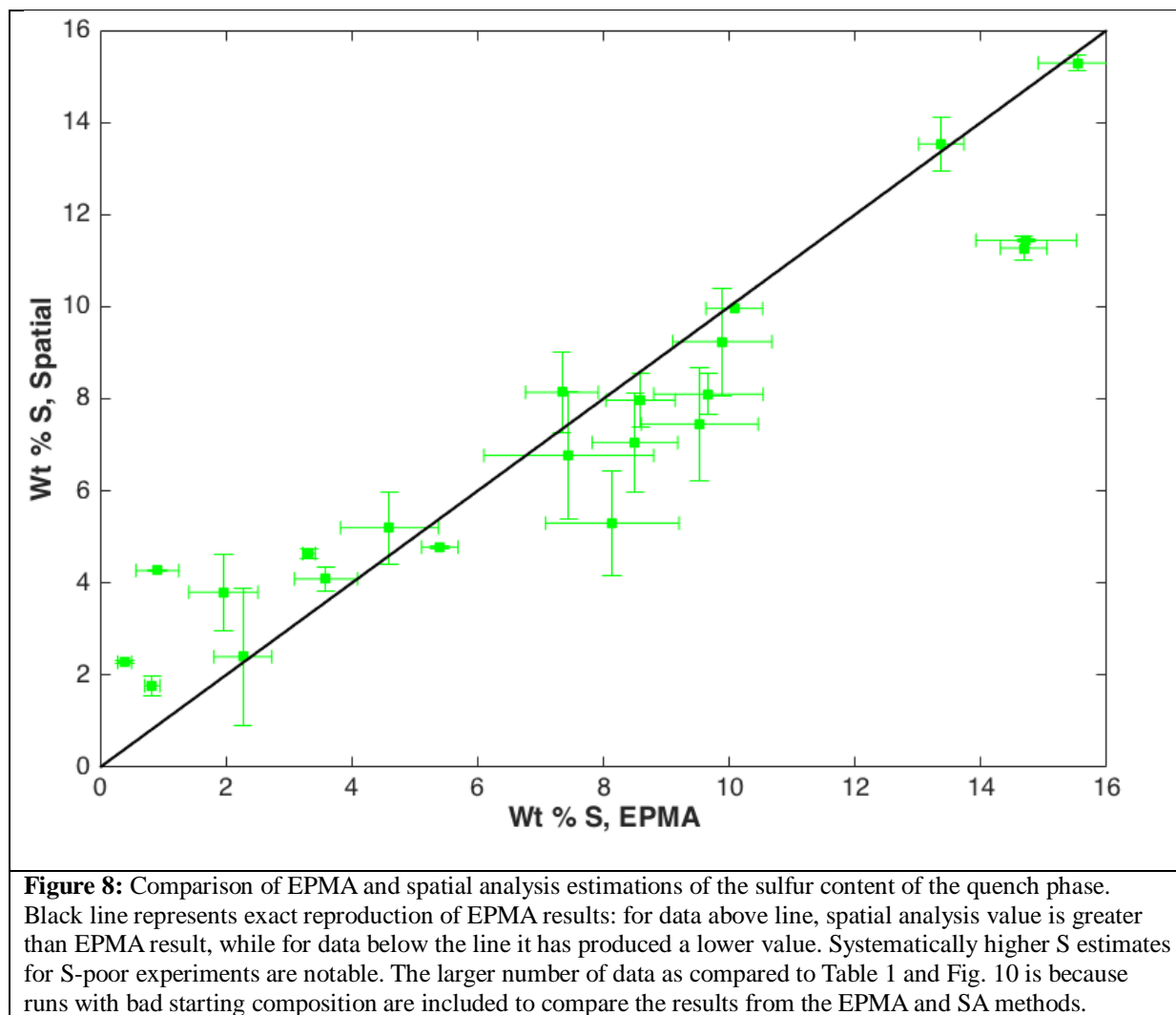


**Figure 7:** Classes resulting from cluster analysis of run M062016. Sources of both images are BSE images in Figs. 5 & 6. Left image was used to determine the fraction of solid, while liquid and dendrite fractions (0.53 & 0.47, respectively) were estimated from the higher magnification, right.

The spatial analysis (SA) technique yields estimates of the quenched liquid phase composition are comparable to EPMA results, deviating an average of 1.3 wt. %. As expected, the SA method resulted in substantially higher estimates for low S runs. While we do not view this method as a substitute for EPMA in all cases, there are certainly applications in this line of research. By allowing us to quickly estimate the composition of our run products, we were able to carry out new experiments without the need to use the electron microprobe, which was frequently unavailable due to constant demand for its use. As we had little idea of the shape of the liquidus at the onset of the project, the ability to keep conducting experiments without pausing to wait for EPMA results was vital in defining the curve in a reasonable amount of time.

SA estimations were also closer to EPMA results than EDS measurements taken with the JEOL SEM, an observation is supported by the literature (Ritchie et al., 2013; Nagoshi et al., 2014). Image classification took a matter of minutes, while the actual processing time for cluster analysis with GIS was only a matter of seconds. This compares quite favorably to EPMA

analysis of the samples, which required an average of two hours per sample, or mapping on the electron microprobe that takes 10's of hours to complete (Carpenter et al., 2013).



We also applied spatial analysis to estimate the bulk composition of the sample. This effort was motivated by a need to see if run product compositions matched our targets for each experiment, as well as a desire to assess the effectiveness of the FeS grain loading method in controlling S content. To this end, the area of the solid phase was also determined, using an

identical procedure and setup as described in Fig. 5. Following this, the fraction of the liquid, dendrite, and solid was determined by dividing their individual areas by their combined totals.

The difference between target compositions and observed compositions are too large to be explained by random errors resulting from aliquot creation (see Suppl. Table). We believe this inconsistency is primarily caused by difficulties in filling the capsules with ~1 mg of uniform material. We loaded sample powder by depositing a small amount on creased weighing paper and coaxing it into the capsule with a needle. A loading rod was then used to pack grains down until the capsule is filled.

The metallic needle, however, proved to be slightly magnetic, which we believe biased the purely powdered samples to higher S-contents by preferentially removing Fe. An initial solution to the problem of the magnetic needle was to vibrate the edges of the weighing paper, without physically touching the powder with a needle. While this eliminated the removal of Fe grains via magnetism, we believe this method also biased the sample against S. We suspect that sliding the grains with the needle preferentially transported the heavier Fe & Ni grains further down the paper's slope. This biased the sample against lighter S by leaving it behind, an effect observed of grain sorting processes at larger scales (Kannan, 2016).

A second solution was the substitution of a braided  $W_{95}Re_5$  thermocouple wire for the needle. We observed that the non-magnetic wire was effective at transporting all compositions of grains with equal ease. One point of concern, however, was significant Re contamination in two of the runs (M090216 & M070216, not represented in Table 1). Contamination could not be explained by interaction of TC wires in the assembly and the sample, so we suspect the Re loading wire may have eventually broken after repeated use and thus contaminated the sample.



Despite these concerns, the Re wires were replaced and used for all other runs without issue, though we advise the use of thicker wires for sample loading.

Unlike the powders, the FeS grains were individually placed in the capsule with tweezers, and thus the magnetic effect of the loading needle was avoided. Additionally, the FeS grains, being large and spherical in comparison to the powders, did not cling to the loading rod. While the Fe-Ni powder was still subject to bias due to the higher relative magnetism of the Fe grains, this partiality had no bearing on the S content and thus had less effect on the overall experimental results, due to Ni's low contribution to the melting temperature of the alloy (Stewart et al., 2007). Comparison of the powder and FeS grain S-control methods via volumetric spatial analysis of run products, however, did not indicate a clear advantage in meeting target compositions, with both methods struggling to consistently meet targets (see Suppl. Table). There was an overall tendency to produce S concentrations that were poorer than intended, which is more favorable than the alternative at high temperature runs.

## Results & Discussion

<b>Table 1:</b> Summary of Experimental Results.							
<i>RunID</i>	<i>T (°C)</i>	<i>Duration</i>	<i>Phase</i>	<i>Fe (wt. %)</i>	<i>Ni (wt. %)</i>	<i>S (wt. %)</i>	<i>Total (wt. %)</i>
<i>M052516</i>	769	24 hr	Solid	87.4(4)	12.2(3)	0.14(3)	99.7(8)
			Solid	94.6(8)	4.1(7)	0.10(4)	98.8(4)
			Fe(Ni) <sub>3</sub> S	77.0(1)	6.08(1)	15.8(1)	98.8(2)
			Fe(Ni) <sub>2</sub> S	73.1(1)	3.5(2)	22.3(1)	98.8(1)
			Fe(Ni) <sub>3</sub> S <sub>2</sub>	68.5(7)	3.5(1)	26.7(3)	99.7(4)
<i>M063016<sub>TC</sub></i>	1000	60 m	Liquid	76.2(9)	9.5(1)	14.7(8)	100.4(2)
			Solid	89.8(4)	9.7(5)	0.39(1)	99.9(1)
<i>M053016</i>	1032	60 m	Liquid	77.4(2)	7.69(3)	14.9(2)	100.0(1)
			Solid	90.7(4)	7.5(1)	0.5(3)	98.7(1)
<i>M020116</i>	1130	4 m	Liquid	74.9(5)	8.8(1)	14.8(5)	98.5(1)
			Solid	89.9(1)	8.69(2)	0.58(2)	99.1(1)
<i>M090116</i>	1137	60 m	Liquid	76.8(4)	8.9(4)	13.4(3)	99.1(1)
			Solid	90.1(1)	8.72(3)	0.311(1)	99.2(1)
<i>M031916</i>	1160	3 m	Liquid	80.9(9)	8.5(1)	9.8(9)	99.1(2)
			Solid	89.6(1)	8.9(1)	0.42(1)	99.1(1)
<i>M021816</i>	1226	2 m	Liquid	81.3(6)	8.7(1)	8.5(7)	99.6(2)
			Solid	90.1(1)	8.7(1)	0.40(3)	99.2(1)
<i>M021116</i>	1298	3 m	Liquid	80.4(8)	9.3(2)	9.5(9)	98.6(1)
			Solid	89.9(1)	9.16(2)	0.309(3)	99.4(1)
<i>M062816</i>	1341	60 m	Liquid	76.3(2)	7.0(1)	15.0(1)	98.4(1)
			Solid	90.4(1)	9.15(1)	0.31(6)	99.8(2)
<i>M062016<sub>TC</sub></i>	1400	60 m	Liquid	80.9(1)*	10.5(1)*	6.8(5)*	98.2(6)*
			Solid	87.5(4)	10.8(1)	0.4(1)	99.1(2)
<i>M022516</i>	1405	1 m	Liquid	82.3(7)	8.9(1)	8.6(6)	99.8(2)
<i>M061816<sub>TC</sub></i>	1500	60 m	Liquid	83.8(4)	10.33(4)	5.4(3)	99.5(2)
			Solid	88.8(1)	10.1(1)	0.189(4)	99.1(1)
<i>M061116<sub>TC</sub></i>	1600	60 m	Liquid	81.1(14)	7.9(1)	9.9(14)	98.9(2)
<i>M062516</i>	1655	60 m	Liquid	87.92(2)*	10.6(1)*	2.6(1)*	101.1(2)*
<i>M061616<sub>TC</sub></i>	1700	60 m	Liquid	82.7(9)	10.5(1)	5.9(9)	99.1(2)
<i>M062616<sub>TC</sub></i>	1719	60 m	Liquid	87.63(4)*	10.9(1)*	3.3(2)*	101.8(4)*
<i>M062916</i>	1769	60 m	Liquid	85.4(2)	14.2(1)	.3(1)	99.9(3)
			Solid	85.3(1)	14.6(1)	0.09(1)	99.9(1)

**Note:** tc denotes a thermocouple run. \* Indicates compositions determined by spatial analysis rather than EPMA. Parenthetical value is uncertainty in last digit(s). For EPMA results, this value is the standard error of the sample of measurements. For spatial analysis results, this value is the combined uncertainty of EPMA standard errors, multiplied by the inverse of the accuracy of the classification of those phases.

The maximum concentration of sulfur in the Fe(Ni) solid is 0.58 ( $\pm$  .02) wt. % in our experiments, much lower than Zhang & Fei's (2008) maximum concentration of 2.72 ( $\pm$  .07) wt. %. While our value is not located at the eutectic, the trend of our solid data indicates this S

deficiency extends across temperatures. This result is in close agreement with Li et al.'s (2001) value of  $.54 (\pm .05 \text{ wt. } \%)$  for Ni-free data at 21 GPa. Additionally, Zhang & Fei's use of 28 - 50 wt. % Ni in their runs, suggests the addition of Ni has a large effect on the concentration of S in the solid. This effect appears to strongly persist at higher pressures as well, as Stewart et al.'s (2007) 23 GPa data for the Fe-Ni-S system features a greater concentration of S in solid Fe(Ni) than Li et al.'s (2001) data for the Fe-S system at 25 GPa.

We posit the primary cause of these discrepancies to be the effect that Ni has on the solid structure of the alloy. In synthesizing a Fe(Ni)S solid for study at higher pressures, Sakai et al. (2012) produced a body-centered cubic (BCC) alloy at 21 GPa. In comparison, at these conditions pure iron exists solidly as a face-centered cubic (FCC) structure. Huang et al. (1988) found that Fe-Ni alloys with 35.1 wt. % Ni are present in the FCC structure at 25 GPa, while alloys with 10.26 & 24.4 wt. % were also observed with BCC & HCP structures. Despite its relatively large ionic radius, S is thought to occupy interstitial sites within the Fe lattice according to the lattice strain model, modified to study metal-metal partitioning (Stewart et al., 2009). BCC & FCC phases feature differing numbers and types of interstitial sites so a structural transition should affect the number of S atoms able to enter the solid.

FCC structures contain eight tetrahedral interstitial sites and thirteen octahedral interstitial sites, while a BCC structure contains 18 octahedral interstitial sites and 4 tetrahedral sites. Octahedral holes are larger than their tetrahedral counterparts, so the BCC structure undergoes less strain to accommodate S atoms than the FCC counterparts. This fact, coupled with BCC's greater number of octahedral sites, suggests that the concentration of S should be higher in this structure than for FCC. As increased Ni improves the stability of the BCC structure versus the FCC, the discrepancy in the concentration of S between our results and the literature suggests

that our data, like Li et al.'s (2001) features solids of FCC structure, while Zhang & Fei (2008) and Stewart et al.'s (2007) results are likely for run products with a BCC solid structure.

In most of our experimental products FeO was present as a dark gray texture in the S-rich interstitial region of the quenched liquid phase (Fig. 3), or as blobs in a manner similar to those Martin et al. (2014) describe in their study of Fe-FeS-Fe<sub>3</sub>C at high pressures. All starting materials were stored in a dehumidifying cabinet prior to use to keep them free from H<sub>2</sub>O, and Raman analysis of their contents did not reveal chemical contamination. Furthermore, all assemblies were kept in a vacuum oven set above 100 °C for at least 1 hour prior to being sintered in the multi-anvil. Pike et al. (1999) found FeO in all sub-solidus experiments, despite the substitution of a BN capsule for some runs, and suggest inherent oxygen fugacity at pressure (18-25 GPa) is to blame. EPMA & EDS revealed that O did not exceed 1 wt. % in any experiment. At this concentration, O is not expected to significantly depress the melting temperature of Fe-S liquidus (Terasaki et al., 2011). Unlike O, H is posited to be the cause of significant melting temperature depression in the Fe-S system (Buono & Walker, 2015). Hydrogen was not detected with Raman or EDS, and our electron microprobe was not equipped to detect its presence. However, we are confident our use of furnaces to dry powders used in the experiments, as well as ovens and sintering to drive off H<sub>2</sub>O was sufficient to keep samples free from the effects of H.

Phases were identified by their chemical compositions, typically derived from EPMA, or EDS in the case of sub-1 μm features. Analysis of the quenched liquid phase determined it to be a combination of Fe-rich dendrite ranging from .32 to .52 wt. % S, and S-rich interstitial liquid ranging from 15.4 to 16.4 wt. % S. EDS analysis of the interstitial liquid microstructures revealed them to be a mixture of solid (bright, spherical texture, Fig. 3) and Fe(Ni)<sub>3</sub>S (darker

texture, Fig. 3). In addition to these runs, our sub-solidus experiment contained five distinct phases,  $\text{Fe}(\text{Ni})_3\text{S}$ ,  $\text{Fe}(\text{Ni})_3\text{S}_2$ ,  $\text{Fe}(\text{Ni})_2\text{S}$ , and two varieties of  $\text{Fe}(\text{Ni})$  solid, a bright phase with Ni content of 12.15 wt. % and a duller phase with 4.1 wt. % Ni. While the number of phases exceeds the amount allowed by the phase rule at all non-eutectic points, we believe that the sluggishness of solid-state kinetics prevented the formation of a single, homogenous solid phase.

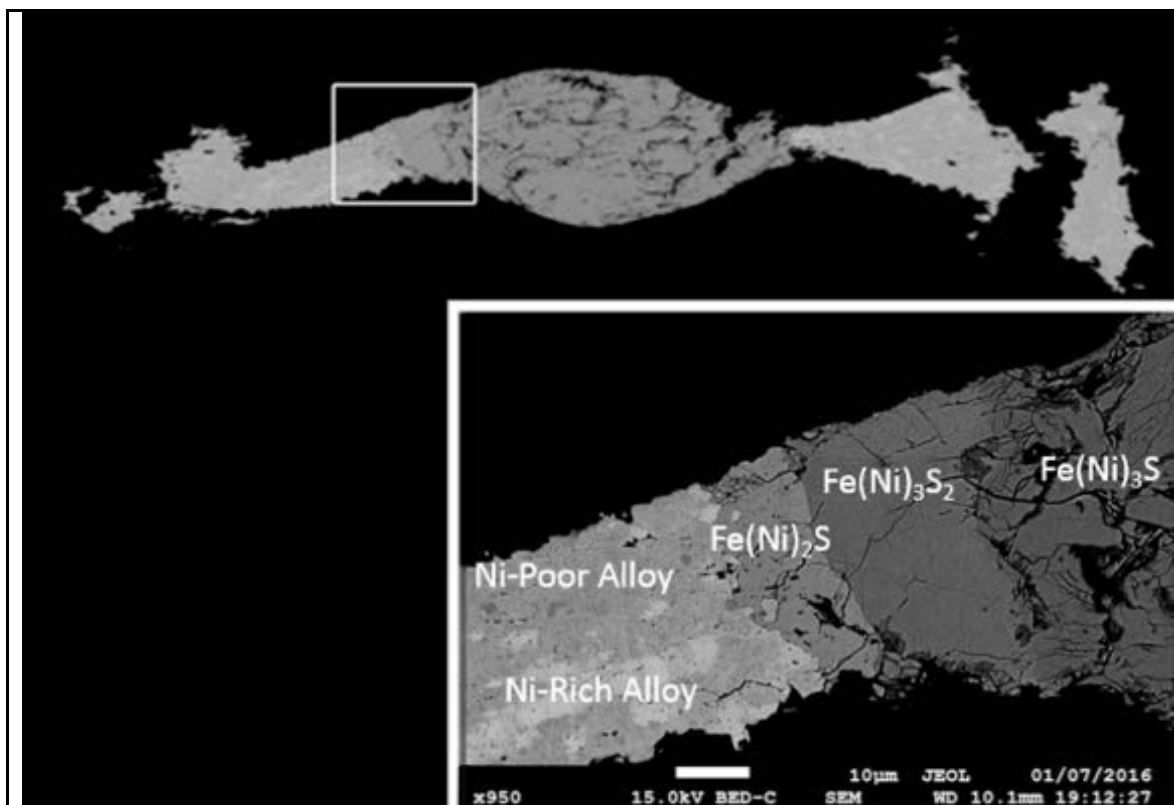


**Figure 9:** BSE image of M052016, our subsolidus run at 733 °C. S is concentrated in the center, reflecting the positioning of  $\text{FeS}$  grains as described in methods. Inset: Dark gray center is  $\text{Fe}(\text{Ni})_3\text{S}$ , medium gray interphase is  $\text{Fe}(\text{Ni})_3\text{S}_2$ , light gray interphase is  $\text{Fe}(\text{Ni})_2\text{S}$ , and lightest mottled region contains two  $\text{Fe}(\text{Ni})$ -rich solids, with bright areas being enriched in Ni (~12 wt. %), and duller areas depleted in Ni (~4wt. %).

The occurrence of  $\text{Fe}(\text{Ni})_2\text{S}$  in our 20 GPa runs contrasts with the first appearance of  $\text{Fe}_2\text{S}$  at 21-22 GPa (Fei et al., 2000; Koch-Müller et al., 2002). Additionally, the presence of  $\text{Fe}(\text{Ni})_2\text{S}$ 's at 769 °C in run M052516 is significantly lower than Fei et al.'s (2000) minimum temperature of 1050 °C for  $\text{Fe}_2\text{S}$  at 21 GPa, indicating Ni significantly lowers its minimum temperature of stability. Both observations are corroborated by Urakawa et al.'s (2011)

conclusion that the addition of Ni broadens the phase stability of Fe-S compounds.

Thermodynamic study of the Fe-Ni-S at 1 bar indicates that increasing Ni content decreases the stability of the Fe(Ni) solid versus the liquid phase, causing a slight depression in melting temperatures (Walder & Pelton, 2004; Raghavan, 2004) that is also observed at higher pressures.

All experimental data, including those of solid phases at the eutectic and pure Fe end-members are plotted in Fig. 10. Anzellini et al.'s (2013) melting experiments to estimate the pure Fe melting temperature, while the eutectic was given by Zhang & Fei's (2008) data. Both were normalized to 9 wt. % Ni by a correction of  $7^{\circ}\text{C}/\text{wt. \% Ni}$  (the average of Zhang & Fei (2008), Stewart et al.'s (2007) and Pike et al.'s melting temperature depressions, resulting in  $2047^{\circ}\text{C}$  and  $940^{\circ}\text{C}$ , respectively). Fitting the data to a 3rd-ordered polynomial results in liquidus that features nearly ideal behavior.

As the Fe-S system exhibits pressure-induced changes in liquidus behavior, we sought a thermodynamic explanation for our melting curve's expression. Inspired by Buono & Walker's (2011) treatment of the Fe-S system from 1-14 GPa, we employed the asymmetric Margules formulation of the Gibbs free energy to examine our system at 20 GPa. The Margules formulation assumes a regular solution, and uses interaction parameters to describe deviations in the mixing behavior of components. Prior to modeling, all sulfur measurements and their accompanying errors were converted from wt. % S to molar fraction FeS. While our experiments contain Ni, we ignore its presence, and instead employ focus on only the Fe and Fe<sub>3</sub>S components.

The asymmetric Margules solution model contains a term for the excess free energy of mixing, represented by interaction parameters  $W_{\text{Fe}}$  and  $W_{\text{FeS}}$ , the compositional end-members of the system. The total free energy of the liquid phase is a sum of that of the liquid Fe and liquid

FeS components, which in turn have contributions from the ideal entropy of mixing, and the non-zero enthalpy of mixing, term 3 below, quantifying the departure from ideal behavior.

$$1) G_{\text{Liq}} = G_{\text{FeLiq}} \cdot (1 - x) + G_{\text{FeSLiq}} \cdot x + x \cdot (1 - x) \cdot [W_{\text{GFe}} \cdot x + W_{\text{GFeS}} \cdot (1 - x)] + R \cdot T \cdot x \cdot \ln(x) + R \cdot T(1 - x) \cdot \ln(1 - x)$$

Where  $R$ ,  $G_{\text{Liq}}$ ,  $G_{\text{FeLiq}}$ ,  $G_{\text{FeSLiq}}$ ,  $W_{\text{GFe}}$ , &  $W_{\text{GFeS}}$  are the gas constant  $\left(\frac{.00831 \text{ kJ}}{\text{mol} \cdot \text{K}}\right)$ ,

Gibbs free energy of the liquid, the Gibbs free energy of liquid iron, the Gibbs free energy of liquid FeS, pure iron's Gibbs interaction parameter, and FeS's Gibbs interaction parameter, respectively.  $T$  is the temperature, in K, produced by our polynomial fit of the data, while  $x$  is our experimental data's sulfur content, in mole fraction FeS. Recalling the definition of the Gibbs free energy, the interaction parameters are themselves broken into sub-components:

$$2) W_{\text{GFe}} = W_{\text{HFe}} + T \cdot W_{\text{SFe}} + W_{\text{VFe}} \cdot P$$

$$W_{\text{GFeS}} = W_{\text{HFeS}} + T \cdot W_{\text{SFeS}} + W_{\text{VFeS}} \cdot P$$

Where  $W_{\text{HFe}}$ ,  $W_{\text{SFe}}$ ,  $W_{\text{VFe}}$ ,  $W_{\text{HFeS}}$ ,  $W_{\text{SFeS}}$ ,  $W_{\text{VFeS}}$ , and  $P$  are the enthalpy interaction parameters of iron, the entropy interaction parameter of iron, the volumetric interaction parameter of iron, the enthalpy interaction parameters of FeS, the entropy interaction parameter of FeS, the volumetric interaction parameter of FeS, and the pressure (20 GPa). As our data is isobaric, the volumetric and pressure terms,  $W_{\text{VFe}}$ ,  $W_{\text{VFeS}}$ , and  $P$  are hereafter ignored. Taking the partial derivative of equation 2 with respect to composition results in:

$$3) \frac{\partial G_{\text{Liq}}}{\partial x} = ((W_{\text{HFeS}} + T \cdot W_{\text{SFeS}} - (G_{\text{FeLiq}} - G_{\text{FeSLiq}})) + 2 \cdot (W_{\text{HFe}} + T \cdot W_{\text{SFe}} - W_{\text{HFeS}} + T \cdot W_{\text{SFeS}}) \cdot x + 3 \cdot (W_{\text{HFeS}} + T \cdot W_{\text{SFeS}} - W_{\text{HFe}} + T \cdot W_{\text{SFe}}) \cdot x + R \cdot T \cdot x \cdot (1 - x)$$

Equation 3 can be simplified by assuming the liquid is at equilibrium with solid Fe, an acceptable generalization due to sulfur's low concentration in Fe at pressures that bracket 20 GPa (Li et al., 2001; Andrault et al., 2009). The reference temperature for solid Fe is given as 1273 K. On a Gibbs free energy-composition plot, this condition is satisfied when the curves of solid Fe and the liquid cross, and a tangent line to this point arrives at the Gibbs free energy of the pure Fe and Fe<sub>3</sub>S end-members.

$$4) \frac{\partial G_{\text{Liq}}}{\partial x} \text{ at equilibrium} = \frac{G_{\text{Liq}} - G_{\text{FeSol}}}{x}$$

Where  $G_{\text{Liq}}$  at equilibrium is the Gibbs free energy of the composite liquid, and  $G_{\text{FeSol}}$  is the Gibbs free energy of solid iron at a fixed pressure and temperature. Using the relationship discussed above, and made discrete in Eq. 4,  $G_{\text{Fe3S}}$  can be substituted out of Eq. 4 in favor of  $G_{\text{Fe}}$ . Thus, Eq. 3 contains only solid and liquid Fe terms, and can be re-arranged in order to regress a 3<sup>rd</sup>-ordered polynomial.

$$5) (G_{\text{FeSol}} - G_{\text{FeLiq}}) = 2(W_{\text{Fe}} - T \cdot W_{\text{Fe3S}}) \cdot x^3 + 2(W_{\text{Fe3S}} - W_{\text{Fe}}) \cdot x^2 + RT \cdot \ln(1 - x)$$

To define the Gibbs free energy of solid and liquid Fe at our experimental conditions, thermodynamic data from Chase (1995) was integrated to the temperatures of interest via the Shomate equation (Shomate, 1954). To solve for  $W_{\text{Fe}}$ ,  $W_{\text{FeS}}$ ,  $W_{\text{Fe}_2\text{S}}$ , &  $W_{\text{Fe}_3\text{S}}$ , the equation was solved with an iterative, linear least squares method.  $T$  was set equal to the temperatures given by our polynomial fit (Fig.13, solid black line), while the Margules parameters were allowed to vary to minimize the difference between the phase boundary conditions observed in our experiments, and  $x$ , and those predicted by the model (Eq. 5). Additionally, an ideal curve was calculated to compare to our experimentally determined liquidus. Two equations of state (EOS)



were used, the Mie Gruneisen and the Birch Murnaghan high temperature equation of state. Both EOS's successfully reproduced our results, with all values for solid and liquid iron derived from Komabayashi & Fei (2010), whose reference conditions of 300 K and atmospheric pressure.

Table 2 summarizes this data, as well as values used the areotherm calculations discussed below.

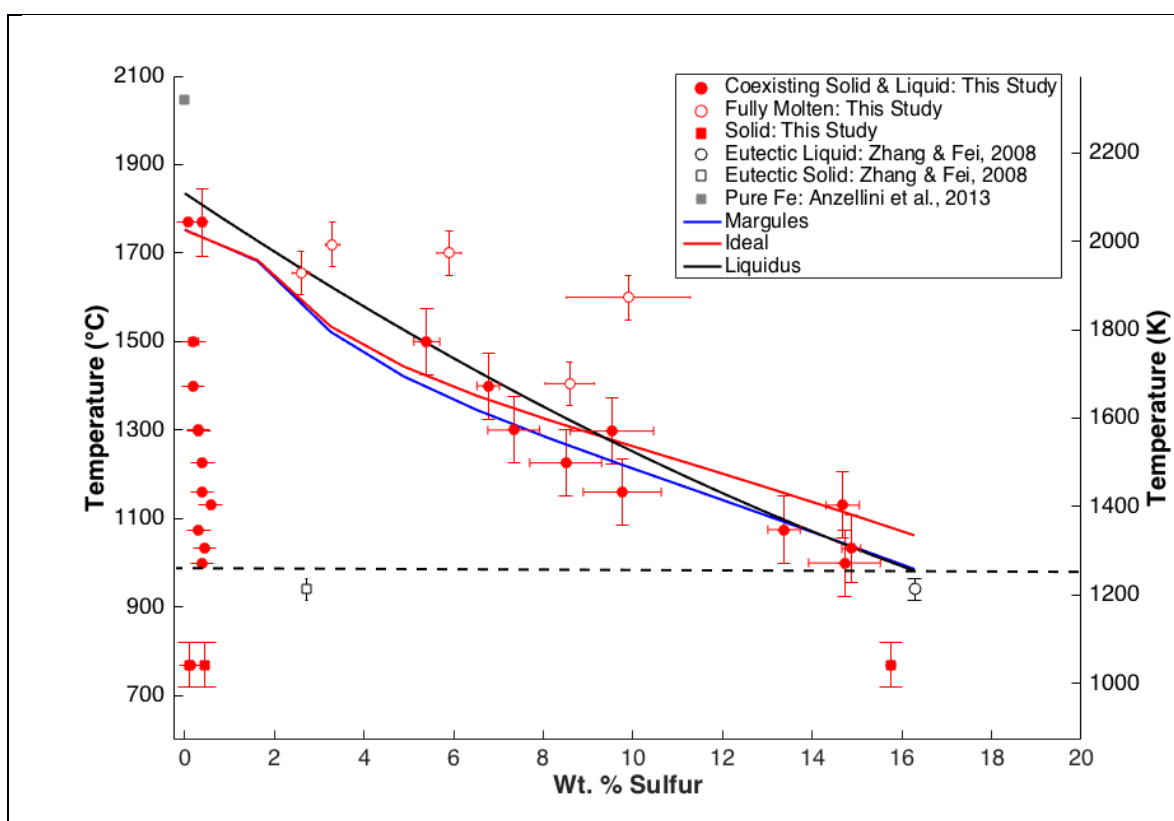


**Figure 10:** Plot of all experimental data, along with fitted liquidus, Margules, and ideal curves. Zhang & Fei's (2008) eutectic result is used to anchor the fit, while Anzellini's melting temperature of pure Fe is presented as a reference. Both the melting temperature of pure Fe and the eutectic data point are normalized to 9 wt. % Ni, with a correction of 7 °C/wt. % Ni (average of depressions observed by Pike et al. (1999), ~8°C/wt. %, Stewart et al., (2007), 3.75°C/wt. %, and Zhang & Fei (2008), 9°C/wt. %). The markers obscure compositional errors smaller than .1 wt.%, and temperature errors for the solid of two-phase runs are omitted for the sake of clarity. Ideal and Margules curves were calculated for the Fe-S binary system, neglecting the presence of Ni.

The liquidus's curvature at 20 GPa closely resembles that of the Fe-S system at 10 GPa (Chen et al., 2008) as well as Andrault et al.'s (2009) limited results for the Si-doped Fe-S system at 20.6 GPa. Deviation from an ideal liquidus is small, but not trivial. For the likely S contents of

the Martian core, temperature depression ranges from a negligible amount at 10 wt. % S to 80 °C at 15 wt. % S. The fact that the Fe-Ni-S system is nearly ideal at 20 GPa appears surprising given the proximity to the stabilization of Fe<sub>3</sub>S at 20 GPa, however there is reason to believe that the addition of Ni has significantly lowered its pressure of initial stability. Pike et al. (1999), who used a starting composition of 6.5 wt. % Ni in contrast to our average of 9 wt. %, observe Fe(Ni)<sub>3</sub>S at 18 GPa. Data on the Ni-S system supports this finding, in that Ni<sub>3</sub>S<sub>2</sub> is observed at atmospheric pressure, as opposed to 14 GPa for Fe<sub>3</sub>S<sub>2</sub> (Fei et al., 1997) while Ni<sub>3</sub>S has been observed at pressures as low as 5.1 GPa (Urakawa et al., 2011). Thus, condition may be enough removed from the stabilization of Fe(Ni)<sub>3</sub>S, that its effects on the liquidus are not felt.

Parameter	W <sub>H</sub> Fe (KJ/mol)	W <sub>H</sub> FeS (KJ/mol)	W <sub>S</sub> Fe (KJ/mol*K)	W <sub>S</sub> FeS (KJ/mol*K)
Value	.82905	.06198	0	3.20584

The slightly positive values of W<sub>H</sub>Fe and W<sub>H</sub>Fe<sub>3</sub>S indicate a small amount of repulsion between the Fe and S in the formation of both end-members. However, Fe's greater values indicate the two phase region will be destabilized closer to this end member, and therefore broader away from it (Dehoff, 2006, Chapter 10). The entropy values are temperature dependent, and Fe<sub>3</sub>S's positive value means its Gibbs free energy is reduced with increasing temperature, thus Fe<sub>3</sub>S becomes increasingly favorable as temperatures decrease. These tendencies cause the liquidus to broaden more rapidly than the solidus, rendering it flat from 10 – 16 wt. % S.

Given the tendency of Ni to stabilize compounds towards lower pressures, and the fact that no new compounds have been discovered in the Fe-S system at pressures above 21 GPa, it is likely that melting behavior in the Fe-Ni-S system remains nearly ideal throughout the domain of Martian core pressures. Thus combining our rigorously defined melting curve with data at higher

pressures should yield interpolations that approximate the evolution of the Martian core's liquidus. The Fe-Ni-S eutectic is constrained at 20 and 23 GPa by Zhang & Fei's (2008) measurements, and at 40 GPa by Stewart et al.'s bracketed solid and two phase data. Under the assumption of a linear relationship between Ni content and temperature depression, Ni-free data from the Fe-S system, as well as Ni rich data were normalized to our average value of 9 wt. % Ni by a correction of 7 °C (see Fig. 10).

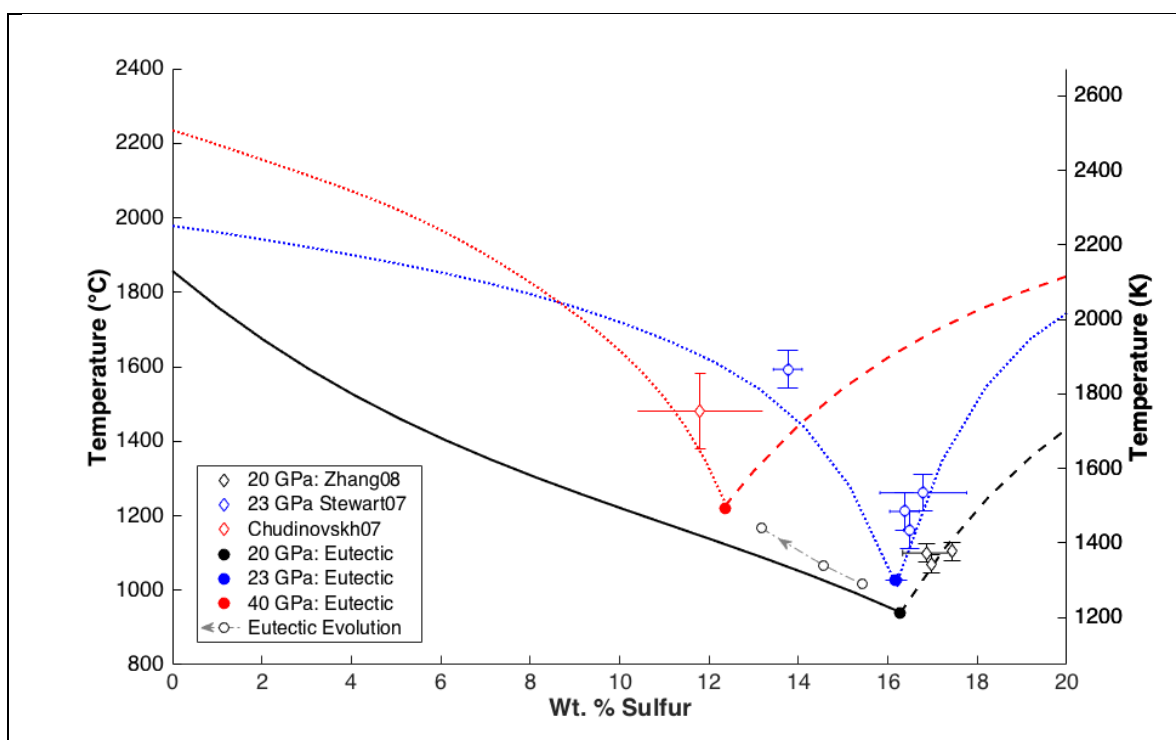


**Figure 11a:** Solid black line is the fit to our 20 GPa data (Fig. 10), and dashed black line is fit to Zhang & Fei's (2008) results. Dotted red and blue lines are liquidii reproduced from Stewart et al. (2007) at 40 GPa and 23 GPa. S-rich liquidii, are represented by dashed blue, red, and black lines, are 2<sup>nd</sup> order power law fits to above data and are anchored by FeS melting temperatures determined by Boehler (1992). Gray points and arrowed line traces evolution of the eutectic increasing from 23 to 31 to 36 GPa (Chudinovskh & Boehler, 2007), whose 40 GPa datum, red diamond, was not used to fit Stewart et al.'s curves but is provided as a supporting reference. 23 GPa eutectic determined by Zhang & Fei (2008) and 40 GPa eutectic bracketed by Stewart et al.'s results for Fe-S and Fe<sub>64</sub>Ni<sub>36</sub>-S.

Stewart et al.'s (2007) initial assessment of the Martian liquidus's evolution with pressure posited concave down liquidus curves based on a limited number of measurements at 23 & 40

GPa. The negative slope between Stewart et al.'s 23 & 40 GPa liquidii determinations is obvious when they are overlaid (Fig 11a.). However, this observation hinges on a single data point taken of the Fe-Ni-S system at 23 GPa, with the 40 GPa melting curve entirely unconstrained by their experiments. In the absence of experimental support, the assumed concave-down liquidii are suspect, given their basis on old assumptions of Fe-S liquidus behavior at lower pressures (Fei & Bertka, 1997) that have subsequently proven to be incorrect (Chen et al., 2008). Given these uncertainties in liquidus shape, we suggest that the negative slope has little experimental basis and may instead be an artifact. However, as Stewart et al.'s results are the only non-eutectic data for the Fe-Ni-S system at these pressures, we intend to briefly explore the consequences.

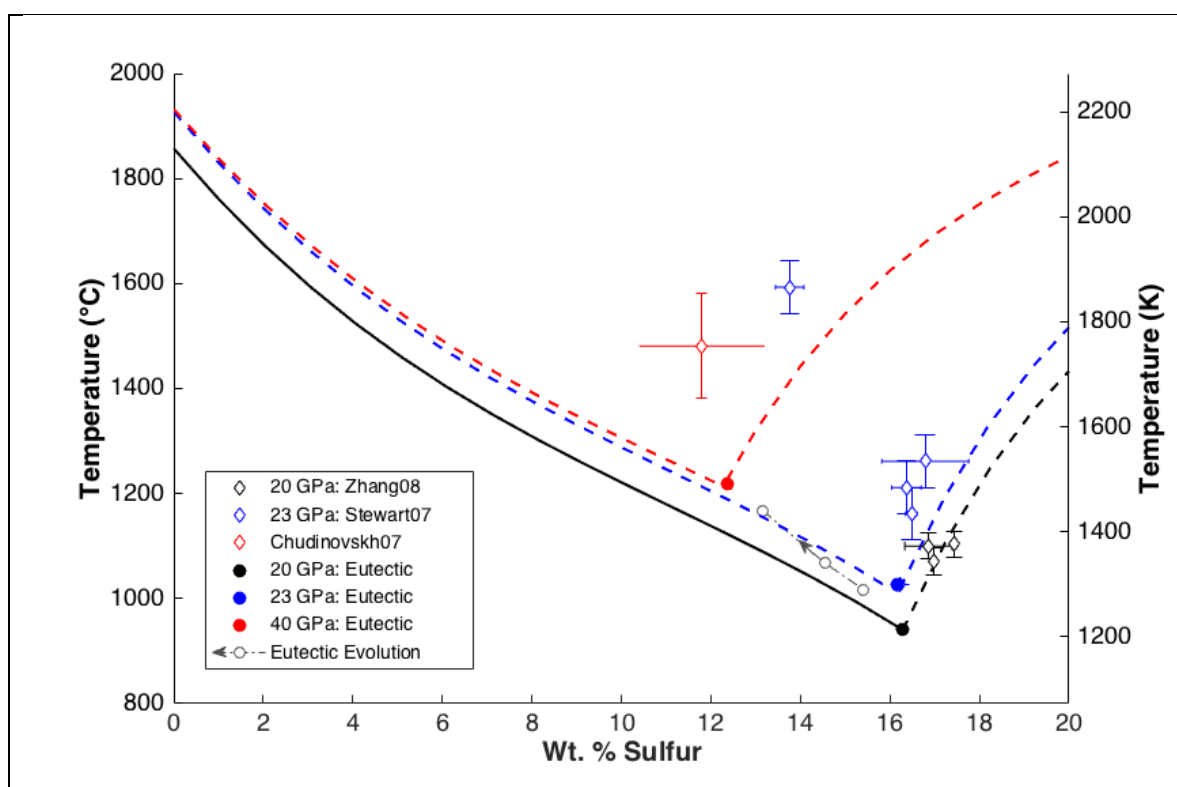


**Figure 11b:** Solid black line is the fit to our 20 GPa data (Fig. 10). Black dashed line is anchored by FeS melting temperatures determined by Boehler (1992) and is a power-law fit to Zhang & Fei's (2008) results, black diamonds and black circle. Liquidii at 20 & 40 GPa, red & blue dashed lines, are translational offsets to 20 GPa data. Gray points and arrowed line traces evolution of the eutectic with pressure from 23 to 31 to 36 GPa (Chudinovskh & Boehler, 2007). Red and blue diamonds are not used to fit lines in this figure, but are included as visual frames of reference to Fig. 11b. 23 GPa eutectic determined by Zhang & Fei (2008) and 40 GPa eutectic bracketed by Stewart et al.'s results for Fe-S and  $\text{Fe}_{64}\text{Ni}_{36}\text{-S}$ .

Based on our results at 20 GPa, we postulate a concave up liquidus persists to greater pressures. Study of the Fe-S system at greater pressures indicates no new solid structures form after Fe<sub>3</sub>S stabilizes at roughly 21-22 GPa (Morard et al., 2007; Fei et al., 2000; Koch-Müller et al., 2002). While our pressures are below this phase boundary, the addition of Ni extends the stability fields of Fe-S compounds to lower pressures (Urakawa et al., 2011), resulting in a revised boundary of 18 GPa (Pike et al., 1999). As Fe(Ni)<sub>3</sub>S is observed in our data set (Run M052516, Table 1), the absence of phase transitions leaves us comfortable extending our experimentally – determined liquidus shape to higher pressures. A prominent feature is the shift in eutectic position of roughly 200 °C and 4 wt. % S from CMB pressures to those at the center of the planet (Chudinovskh & Boehler, 2007). As a result, the liquidus is considerably steeper on the S-rich side of the eutectic, meaning that intersection with the areotherm likely occurs at high pressures (Stewart et al., 2007). ).

An additional facet to is that a given core composition may cross from one side of the eutectic to the other with pressure. The result is that cores with S contents above 12 wt. % shift from the Fe-rich side of the liquidus near the CMB to the S-rich side at the planet's center. This affects the core liquidii by producing a pressure-induced jump in temperature at these compositions. With the liquidii at 20 GPa from this study, and those at 23, & 40 GPa given in the literature, we calculated core areotherms representative of our end-members of 10 wt. % and 16 wt. % S, hereafter referred to as A10 and A16, respectively. For the sake of brevity, in the following discussion we use only the values employed for the A16, unless explicitly stated. These numbers, as well as those used in the calculation of the 16 wt. % areotherm, are found in Table 2. Assuming the core is well-mixed and defined by constant entropy, we treat the areotherm as an adiabatic gradient such that:

$$6) \frac{dT}{dP} = \frac{\alpha \cdot T \cdot Vm}{\rho \cdot Cp}$$

Where  $\alpha$  is the thermal expansion,  $T$  is the temperature,  $\rho$  is the pressure-dependent density,  $Vm$  is the molar volume, and  $Cp$  is the constant-pressure heat capacity. A  $Cp$  value of 50.615 J/molK was obtained by a weighted average of the pure iron value, 46.024 J/molK and the FeS value of 62.551 J/molK (Chase, 1998) for 1723 °C, the estimated temperature of the CMB (Williams & Nimmo, 2004). The 3<sup>rd</sup> order Birch Murnaghan EOS was employed to determine  $\rho$  at pressure:

$$7) P = \frac{3}{2} K_T \left[ \left( \frac{\rho}{\rho_{OT}} \right)^{\frac{7}{3}} - \left( \frac{\rho}{\rho_{OT}} \right)^{\frac{5}{3}} \cdot \left\{ 1 + \frac{3}{4} (K'_{T_0} - 4) \left[ \left( \frac{\rho}{\rho_{OT}} \right)^{\frac{2}{3}} - 1 \right] \right\} \right]$$

Where  $P$ ,  $K_T$ ,  $\rho_{OT}$ , and  $K'_{T_0}$ , are the pressure of interest, bulk modulus, zero pressure density, and pressure derivative of the bulk modulus. A  $K'_{T_0}$  value of 4.8 is given by Balog et al. (2003).

The bulk modulus increases slightly with temperature, formulated as:

$$8) K_T = K_{T_0} + \left( \frac{\partial K_T}{\partial T} \right)_P \cdot (T - T_0)$$

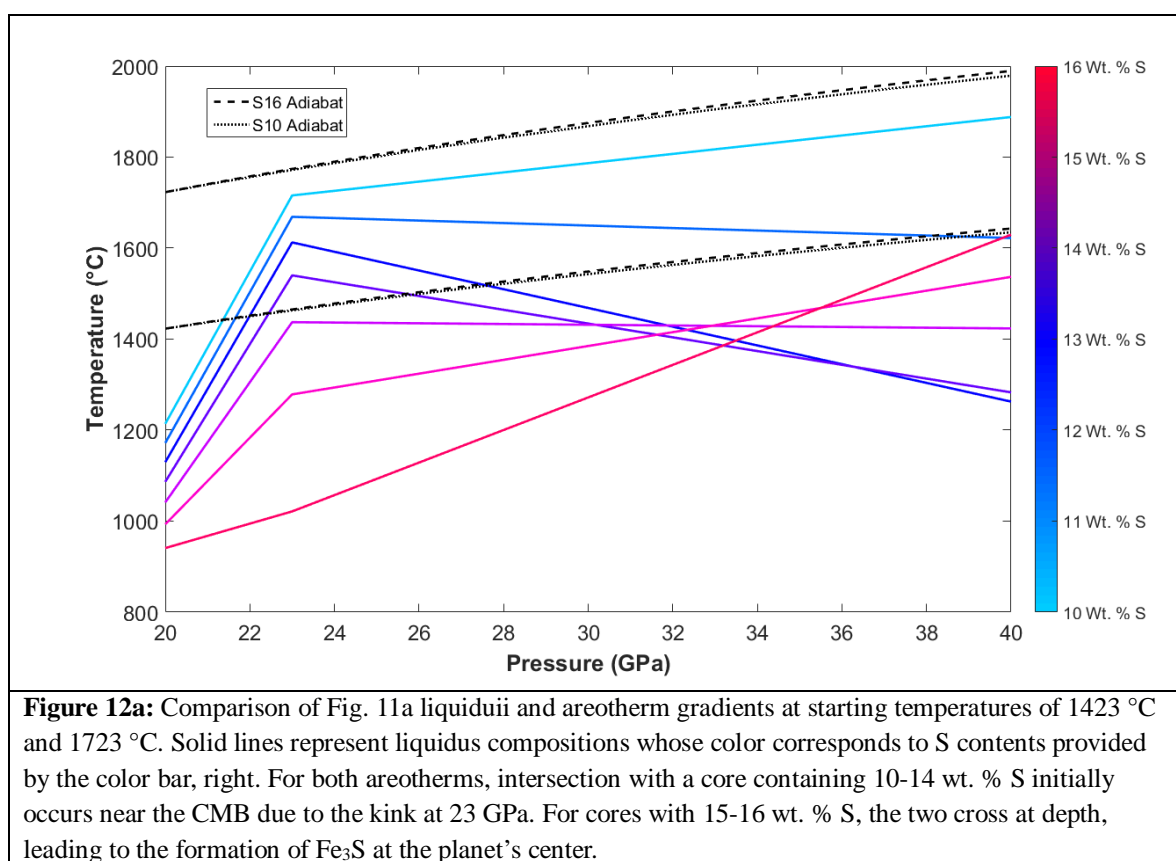
$K_{T_0}$ , the zero temperature bulk modulus at the pressure of interest, is calculated by combining  $K'_{T_0}$  with the ambient density of 45 GPa (Sanloup et al., 2002). Hixson et al.'s (1990) value was used for  $(\partial K_T / \partial T)_P$ , the temperature dependence of the bulk modulus.  $T_0$  is the reference temperature, corresponding to 1377 °C, the temperature of Sanloup et al.'s (2002) experiments. The temperature-dependent zero pressure density is given as:

$$9) \rho_{OT} = \rho_0 \exp \left[ \int_{T_0}^T \alpha_0 dT \right]$$

Where  $\rho_0$  is 5,200 kg/m<sup>3</sup> (Sanloup et al., 2003) and  $\alpha_0$  is the zero pressure thermal expansion coefficient. Following the advice of Williams (2009) a thermal expansion value of  $13.2 \times 10^{-5}/K$  (Assael et al., 2006) was used for liquid iron, which was combined with  $1.7 \times$



Their similar gradient demonstrates the Martian areotherm is insensitive to small to moderate changes in S. Significantly, both are lower than the adiabat applied to the Martian core by Fei & Bertka (2005) an effect that is magnified at depth. For a CMB temperature of 1723 °C, A10 decreases in slope from 17.5°C/GPa at the CMB to 9.9 °C/GPa at the center, while A16 decreases from, 18.4°C/GPa at the CMB to only 10.2 °C/GPa at Mars's center. For a CMB temperature of 1423 °C, A10 decreases in slope from 14.5 °C/GPa at the CMB to 8 °C/GPa at the center, while A16 decreases from, 15°C/GPa at the CMB to only 8.4°C/GPa at Mars's center. Shallowing the areotherm has the effect of causing initial with the liquidus at higher pressures.



All of Stewart et al.'s liquidii are consistent with a CMB temperature of 1723 °C, although the pronounced kink at 23 GPa results in a lower bound of ~1700 °C corresponding to a 10 wt. % S core. An abrupt change in liquidus slope is also observed by Chen et al. (2008) at



14 GPa, yet there is no evidence for a phase transition at 23 GPa that might explain this behavior. For a CMB temperature of 1423 °C, only cores with 14 or 15 wt. % S are located at or above the areotherm, meaning the rest would have begun solidifying. If we consider Stewart et al.'s (2007) initial assessment of the 40 GPa melting curve to be accurate, most liquidii would cross the areotherm near the CMB, resulting in iron snow, while the 15 & 16 wt. % liquidii initially cross the areotherm at the planet's center, producing bottom-up crystallization of Fe<sub>3</sub>S.

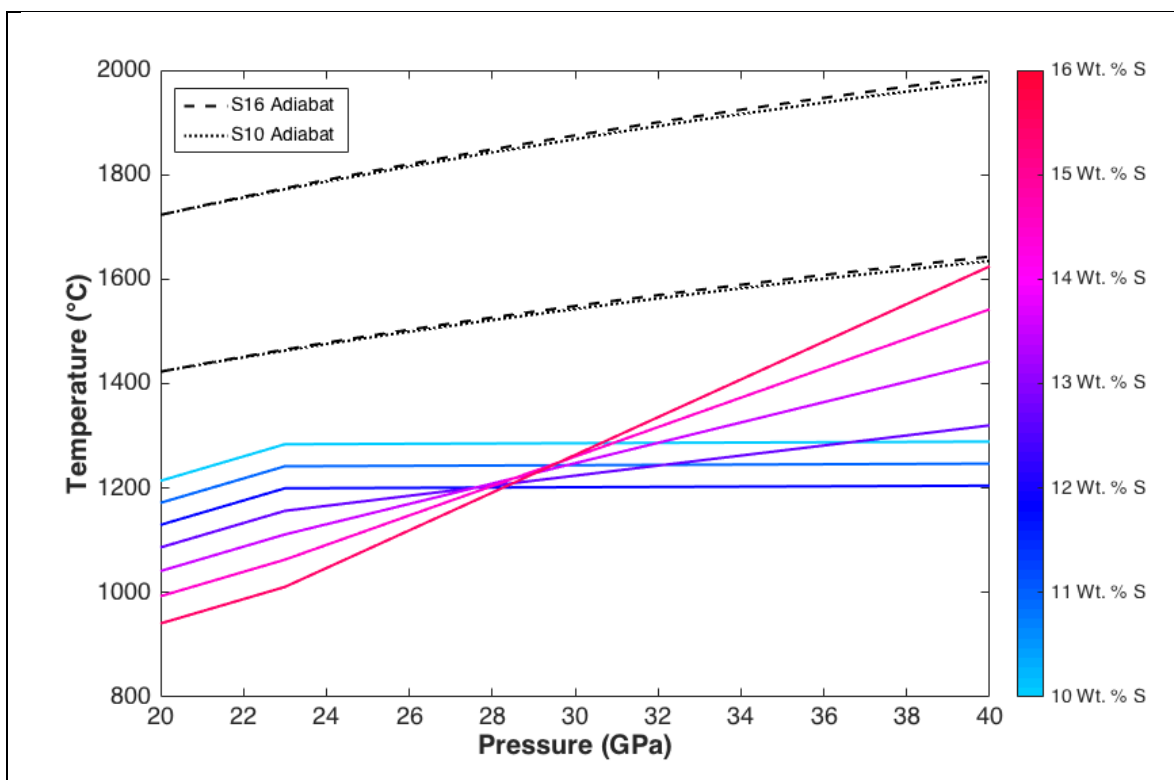


**Figure 12b:** Comparison of Fig. 11b liquidii and areotherm gradients at starting temperatures of 1423 °C and 1723 °C. For both areotherms, intersection with a core containing 10-12 wt. % S occurs near the CMB, resulting in the crystallization of iron snow. For cores with 13-16 wt. % S, the two cross at depth, leading to the formation of Fe<sub>3</sub>S at the planet's center.

Our liquidus constructions are completely consistent with a molten core for the estimated CMB temperature range of 1423 to 1723 °C. As such, they define new lower temperature limits the core can exist at prior to the onset of solidification. These range from 1610 °C, corresponding to a core with 16 wt. % and a CMB temperature of 1423 °C to 1205 °C for a core with 10 wt. % S. Comparison of core areotherms and our liquidii (Fig. 12b) show that a core with 10-12 wt. %

S will initially crystallize near the kink at 23 GPa in the form of iron snow. When the iron snow sinks and dissolves, it enriches the surrounding melt in Fe, creating a higher density layer above the undisturbed, lighter core below (Breuer et al., 2015). As this density inversion is unstable, large-scale compositional overturn eventually occurs, and the heat dissipated by sinking iron is thought to be sufficient to drive a dynamo (Zhan & Schubert, 2012). Interestingly, the kink also opens up the possibility of a dynamo above the snowing layer, as latent heat released by the solidification of Fe, as well as liberated S would rise, stimulating convection in the core up until the CMB at 20 GPa. In the case of 10 wt. % S, top-down formation of Fe snow would be quickly accompanied by bottom-up crystallization of Fe in a manner similar to Earth. Crystallization of Fe cause heat and S-rich fluid to rise through the core providing a more stable source of energy for the dynamo that avoids the risk of compositional stratification (Laneuville et al., 2014)

Cores with 13-16 wt. % S experience initial solidification at depth, leading to the formation of  $\text{Fe}_3\text{S}$  at the planet's center. Since  $\text{Fe}_3\text{S}$  is more dense than the remaining core liquid (Stewart et al., 2007), it is expected to remain at the center of Mars upon crystallization, providing a steady source of heat as the compositional domain at sub-areotherm temperatures extends to lesser depths as the core grows outward. Interestingly, our 13 wt. % liquidus is nearly parallel to the calculated areotherms, so given cooling the two would intersect at multiple depths, leading to solidification throughout the Martian core, including of  $\text{Fe}_3\text{S}$  snow at depths greater than  $\sim 36$  GPa. Doubly snowing cores with conflicting dipole orientations and are thought to explain the surprisingly weak field observed around Mercury (Vilim et al., 2010). If snow is occurring at multiple depths in Mars, evidence of the resulting weak field might be shielded by the mantle, which is much thicker than Mercury's, opening up the possibility that core solidification has already begun.

## Conclusion

Stewart et al.'s liquidus temperatures are too high to be compatible with estimates of the Martian areotherm, given a non-solidifying core. The especially high temperatures at 23 GPa produce an abnormally high temperature gradient when interpolated to our data at 20 GPa. If trends in the evolution of solid and liquid FeS with pressure are accurate (Morard et al. 2007; Li et al., 2001) the change in concavity between the two pressures is difficult to explain. Additionally, the melting curve results are inconsistent with most estimations of the CMB temperature, as well as our determination of the Martian core areotherm. These observations, combined with the dubious construction of the liquidii, suggest that Stewart et al.'s 23 GPa are not reliable predictors of the state of the Martian core. While we are confident in our liquidus determination, and are optimistic its shape persists to greater depths, additional, non-eutectic melting data is needed at to get a comprehensive understanding of the Martian core's state.

Applying surface-based determinations of 300 °C/Ga for the cooling rate of the Martian core (Ruiz, 2014; Lessel & Putirka, 2015) to the results of Fig 12. For a CMB temperature of 1773 °C the most optimistic estimate for compositions currently below the areotherm is that Mars will require 193 million years to initiate crystallization, with pessimistic estimates stretch to over 1 billion years, perhaps even longer if reverse-fault analysis is accurate (Nahm et al., 2011). However, the thermal state of the planet remains very poorly constrained. If, instead, the Martian CMB is at 1423 °C and its core is S-rich, Mars would be significantly closer to the onset of solidification, and may even house a hidden dynamo if solidification is occurring at multiple depths. New data, particularly seismic as well as high-pressure melting data, is required to better define the Martian core across its pressure, temperature, and compositional conditions.

By experimentally defining the Fe-Ni-S melting curve at Martian core conditions, and calculating liquidus and adiabatic gradients across its pressure domain, we have improved the knowledge of its current and future status. Our work highlights the importance of using accurate thermodynamic values and starting materials in gaining the most detailed and nuanced understanding of natural systems. Spatial analysis proved to be a powerful tool in estimating the compositions of fine textures to a high degree of accuracy, while S content control remains a challenge at high temperatures and pressures. We hope this work raises questions about our understanding of other planetary bodies, and encourages others to put hypothesis to the test through experimentation.

Most evidence indicates the Martian core is in a "Goldilocks" state: long since too cool for thermal convection, but too warm for solidification-driven chemical convection to begin. If core crystallization does occur, it is more likely to do so from the bottom up, giving Martian more in common with larger bodies like Earth and the gas giants than the smaller planets and moons. While Mars may not begin forming an inner core in the near future, there are undoubtedly planets in our galaxy that share many of its characteristics. Knowledge of the Martian core is critical to predict the habitability of similar planets, with older and therefore cooler worlds more likely to have regenerated dynamos capable of producing the magnetic fields that shelter life.

## References

- Acuna, M.H., Connerney, J.E.P., Lin, R.P., Mitchell, D., Carlson, C.W., McFadden, J., Anderson, K.A., Rème, H., Mazelle, C., Vignes, D. and Wasilewski, P., (1999). Global distribution of crustal magnetization discovered by the Mars Global Surveyor MAG/ER experiment. *Science*, 284(5415), pp.790-793.
- Aesar, A., (2007). Research Chemicals. *Metals and Materials*, p.196.
- Anderson, K.A., Rème, H., Mazelle, C., Vignes, D. and Wasilewski, P., (1999). Global distribution of crustal magnetization discovered by the Mars Global Surveyor MAG/ER experiment. *Science*, 284(5415), pp.790-793.
- Andraut, D., Bolfan-Casanova, N., Ohtaka, O., Fukui, H., Arima, H., Fialin, M., & Funakoshi, K. (2009). Melting diagrams of Fe-rich alloys determined from synchrotron in situ measurements in the 15–23GPa pressure range. *Physics of the Earth and Planetary Interiors*, 174(1), 181-191.
- Anzellini, S., Dewaele, A., Mezouar, M., Loubeyre, P. and Morard, G., (2013). Melting of iron at Earth's inner core boundary based on fast X-ray diffraction. *Science*, 340(6131), pp.464-466.
- Assael, M. J., Kakosimos, K., Banish, R. M., Brillo, J., Egry, I., Brooks, R., ... & Wakeham, W. A. (2006). Reference data for the density and viscosity of liquid aluminum and liquid iron. *Journal of physical and chemical reference data*, 35(1), 285-300.
- Balog, P. S., Secco, R. A., Rubie, D. C., & Frost, D. J. (2003). Equation of state of liquid Fe-10 wt% S: Implications for the metallic cores of planetary bodies. *Journal of Geophysical Research: Solid Earth*, 108(B2).

- Bertka, C. M., & Fei, Y. (1998). Density profile of an SNC model Martian interior and the moment-of-inertia factor of Mars. *Earth and Planetary Science Letters*, 157(1), 79-88.
- Birch, F. (1968). On the possibility of large changes in the Earth's volume. *Physics of the Earth and Planetary Interiors*, 1(3), 141-147.
- Boehler, R. (1992). Melting of the Fe-FeO and the Fe-FeS systems at high pressure: constraints on core temperatures. *Earth and Planetary Science Letters*, 111(2), 217-227.
- Brandon, A. D., Puchtel, I. S., Walker, R. J., Day, J. M., Irving, A. J., & Taylor, L. A. (2012). Evolution of the martian mantle inferred from the  $^{187}\text{Re}$ – $^{187}\text{Os}$  isotope and highly siderophile element abundance systematics of shergottite meteorites. *Geochimica et Cosmochimica Acta*, 76, 206-235.
- Breuer, D., Rueckriemen, T., & Spohn, T. (2015). Iron snow, crystal floats, and inner-core growth: modes of core solidification and implications for dynamos in terrestrial planets and moons. *Progress in Earth and Planetary Science*, 2(1), 1.
- Buono, A. S., & Walker, D. (2011). The Fe-rich liquidus in the Fe–FeS system from 1bar to 10GPa. *Geochimica et Cosmochimica Acta*, 75(8), 2072-2087.
- Buono, A.S. and Walker, D., (2015). H, not O or pressure, causes eutectic T depression in the Fe-FeS System to 8 GPa. *Meteoritics & Planetary Science*, 50(4), pp.547-554.
- Carpenter, P. K., North, S. N., Jolliff, B. L., & Donovan, J. J. (2013, March). EPMA Quantitative Compositional Mapping and Analysis of Lunar Samples. In *Lunar and Planetary Science Conference* (Vol. 44, p. 1827).
- Chabot, N.L., McDonough, W.F., Jones, J.H., Saslow, S.A., Ash, R.D., Draper, D.S., Agee, C.B., (2011). Partitioning behavior at 9 GPa in the Fe-S system and implications for planetary evolution. *Earth Planet Sc Lett* 305, 425-434.

- Chase Jr, M. W., Davies, C. A., Downey Jr, J. R., Frurip, D. J., McDonald, R. A., & Syveraud, A. N. (1985). JANAF thermodynamic tables. *J. Phys. Chem. Ref. Data*, 14(Suppl. 1), 1.
- Chen, B., Gao, L., Funakoshi, K. I., & Li, J. (2007). Thermal expansion of iron-rich alloys and implications for the Earth's core. *Proceedings of the National Academy of Sciences*, 104(22), 9162-9167.
- Chen, B., Li, J., & Hauck, S. a. (2008). Non-ideal liquidus curve in the Fe-S system and Mercury's snowing core. *Geophysical Research Letters*, 35(7), 10–14.
- Chudinovskikh, L., & Boehler, R. (2007). Eutectic melting in the system Fe–S to 44 GPa. *Earth and Planetary Science Letters*, 257(1), 97-103.
- DeHoff, R. (2006). *Thermodynamics in materials science*. CRC Press.
- Duffy, T. S., & Ahrens, T. J. (1993). Thermal expansion of mantle and core materials at very high pressures. *Geophysical Research Letters*, 20(11), 1103-1106.
- Dumberry, M., & Rivoldini, A. (2015). Mercury's inner core size and core-crystallization regime. *Icarus*, 248, 254-268.
- Fassett, C. I., & Head, J. W. (2011). Sequence and timing of conditions on early Mars. *Icarus*, 211(2), 1204-1214.
- Fei, Y., Bertka, C.M., Finger, L.W., (1997). High-Pressure Iron-Sulfur Compound, Fe<sub>3</sub>S<sub>2</sub>, and Melting Relations in the Fe-FeS System. *Science*, 275(5306), 1621–1623.
- Fei, Y. and Bertka, C., (2005). The interior of Mars. *Science*, 308(5725), pp.1120-1121.
- Fei, Y., Li, J., Bertka, C.M. and Prewitt, C.T., (2000). Structure type and bulk modulus of Fe<sub>3</sub>S, a new iron-sulfur compound. *American Mineralogist*, 85(11-12), pp.1830-1833.

- Gopon, P., Fournelle, J., Llovet, X. and Sobol, P., (2012), December. Low Voltage EPMA of Lunar, Terrestrial, and Synthetic Fe-Si Compounds. In *AGU Fall Meeting Abstracts* (Vol. 1, p. 06).
- Grande, J. C. (2000). Principles of image analysis. *Metallography, Microstructure, and Analysis*, 1-17.
- Hauck, S. a., Aurnou, J. M., & Dombard, A. J. (2006). Sulfur's impact on core evolution and magnetic field generation on Ganymede. *Journal of Geophysical Research E: Planets*, *111*(9), 1–14.
- Hauck, S.A. and Phillips, R.J., 2002. Thermal and crustal evolution of Mars. *Journal of Geophysical Research: Planets*, *107*(E7).
- Hixson, R. S., Winkler, M. A., & Hodgdon, M. L. (1990). Sound speed and thermophysical properties of liquid iron and nickel. *Physical Review B*, *42*(10), 6485.
- Hori, K., & Wicht, J. (2013). Subcritical dynamos in the early Mars' core: Implications for cessation of the past Martian dynamo. *Physics of the Earth and Planetary Interiors*, *219*, 21-33.
- Huang, E., Bassett, W. A., & Weathers, M. S. (1988). Phase relationships in Fe-Ni alloys at high pressures and temperatures. *Journal of Geophysical Research: Solid Earth*, *93*(B7), 7741-7746.
- Jing, Z.C., Wang, Y.B., Kono, Y., Yu, T., Sakamaki, T., Park, C., Rivers, M.L., Sutton, S.R., Shen, G.Y., (2014). Sound velocity of Fe-S liquids at high pressure: Implications for the Moon's molten outer core. *Earth Planet Sc Lett* *396*, 78-87.



- Kannan, A. S., Lassen, N. C. K., Carstensen, J. M., Lund, J., & Sasic, S. (2016). Segregation phenomena in gravity separators: A combined numerical and experimental study. *Powder Technology*, *301*, 679-693.
- Kaiura, G. H., & Toguri, J. M. (1979). Densities of the molten FeS, FeS–Cu<sub>2</sub>S and Fe–S–O systems—utilizing a bottom-balance Archimedean technique. *Canadian Metallurgical Quarterly*.
- Ke, Y., & Solomatov, V. S. (2009). Coupled core-mantle thermal evolution of early Mars. *Journal of Geophysical Research E: Planets*, *114*(7), 112.
- Khan, a, & Connolly, J. a D. (2008). Constraining the composition and thermal state of Mars from inversion of geophysical data. *Journal of Geophysical Research*, *113*, E07003.
- Koch-Müller, M., Fei, Y., Wirth, R., & Bertka, C. M. (2002, March). Characterization of high-pressure iron-sulfur compounds. In *Lunar and Planetary Science Conference* (Vol. 33, p. 1424).
- Komabayashi, T., & Fei, Y. (2010). Internally consistent thermodynamic database for iron to the Earth's core conditions. *Journal of Geophysical Research: Solid Earth*, *115*(B3).
- Konopliv, A. S., Asmar, S. W., Folkner, W. M., Karatekin, Ö., Nunes, D. C., Smrekar, S. E., ... & Zuber, M. T. (2011). Mars high resolution gravity fields from MRO, Mars seasonal gravity, and other dynamical parameters. *Icarus*, *211*(1), 401-428.
- Kuang, W., Jiang, W. and Wang, T., (2008). Sudden termination of Martian dynamo?: Implications from subcritical dynamo simulations. *Geophysical Research Letters*, *35*(14).
- Laneuville, M., Wieczorek, M. A., Breuer, D., Aubert, J., Morard, G., & Rückriemen, T. (2014). A long-lived lunar dynamo powered by core crystallization. *Earth and Planetary Science Letters*, *401*, 251-260.

- Leinenweber, K.D., Tyburczy, J.A., Sharp, T.G., Soignard, E., Diedrich, T., Petuskey, W.B., Wang, Y. and Mosenfelder, J.L., (2012). Cell assemblies for reproducible multi-anvil experiments (the COMPRES assemblies). *American Mineralogist*, 97(2-3), pp.353-368.
- Lessel, J., & Putirka, K. (2015). New thermobarometers for martian igneous rocks, and some implications for secular cooling on Mars. *American Mineralogist*, 100(10), 2163-2171.
- Li, J., Fei, Y., Mao, H. K., Hirose, K., & Shieh, S. R. (2001). Sulfur in the Earth's inner core. *Earth and Planetary Science Letters*, 193(3), 509-514.
- Li, Y., Onasch, C.M. and Guo, Y., (2008). GIS-based detection of grain boundaries. *Journal of Structural Geology*, 30(4), pp.431-443.
- Lin, J.F., Fei, Y., Sturhahn, W., Zhao, J., Mao, H.K. and Hemley, R.J., (2004). Magnetic transition and sound velocities of Fe<sub>3</sub>S at high pressure: Implications for Earth and planetary cores. *Earth and Planetary Science Letters*, 226(1), pp.33-40.
- Lodders, K., & Fegley, B. (1997). An oxygen isotope model for the composition of Mars. *Icarus*, 126(2), 373-394.
- Martin, A. M., Van Orman, J., Hauck, I. I., Steven, A., Chen, B., Sun, N., ... & Han, J. C. W. (2014). *In situ determination of the eutectic melting temperature of Fe-FeS-Fe<sub>3</sub>C between 4.5 and 24.5 GPa and implications for Mercury's core*. Advanced Photon Source (APS), Argonne National Laboratory (ANL), Argonne, IL (US).
- Merlet, C., & Llovet, X. (2012). Uncertainty and capability of quantitative EPMA at low voltage? A review. In *IOP Conference Series: Materials Science and Engineering* (Vol. 32, No. 1, p. 012016). IOP Publishing.

- Mitchell, D. L., Lin, R. P., Mazelle, C., Rème, H., Cloutier, P. A., Connerney, J. E. P., ... & Ness, N. F. (2001). Probing Mars' crustal magnetic field and ionosphere with the MGS Electron Reflectometer. *Journal of Geophysical Research: Planets*, 106(E10), 23419-23427.
- Morard, G., Andrault, D., Guignot, N., Siebert, J., Garbarino, G., & Antonangeli, D. (2011). Melting of Fe–Ni–Si and Fe–Ni–S alloys at megabar pressures: implications for the core–mantle boundary temperature. *Physics and Chemistry of Minerals*, 38(10), 767-776.
- Morard, G., Sanloup, C., Fiquet, G., Mezouar, M., Rey, N., Poloni, R., & Beck, P. (2007). Structure of eutectic Fe-FeS melts to pressures up to 17GPa: Implications for planetary cores. *Earth and Planetary Science Letters*, 263(1-2), 128 -139.
- Nagoshi, M., & Sato, K. (2014). SEM-EDS with low primary electron energy as a tool of surface analysis. *Surface and Interface Analysis*, 46(10-11), 865-868.
- Nahm, A. L., & Schultz, R. a. (2011). Magnitude of global contraction on Mars from analysis of surface faults: Implications for martian thermal history. *Icarus*, 211(1), 389–400.
- Pike, W. A., Bertka, C. M., & Fei, Y. (1999, March). Melting Temperatures in the Fe-Ni-S System at High Pressures: Implications for the State of the Martian Core. In *Lunar and Planetary Science Conference* (Vol. 30, p. 1489).
- Raghavan, V., (2004). Fe-Ni-S (iron-nickel-sulfur). *Journal of phase equilibria and diffusion*, 25(4), pp.373-381.
- Rai, N., & Van Westrenen, W. (2013). Core-mantle differentiation in Mars. *Journal of Geophysical Research E: Planets*, 118(January), 1195–1203.
- Righter, K. and Chabot, N.L., (2011). Moderately and slightly siderophile element constraints on the depth and extent of melting in early Mars. *Meteoritics & Planetary Science*, 46(2), pp.157-176.

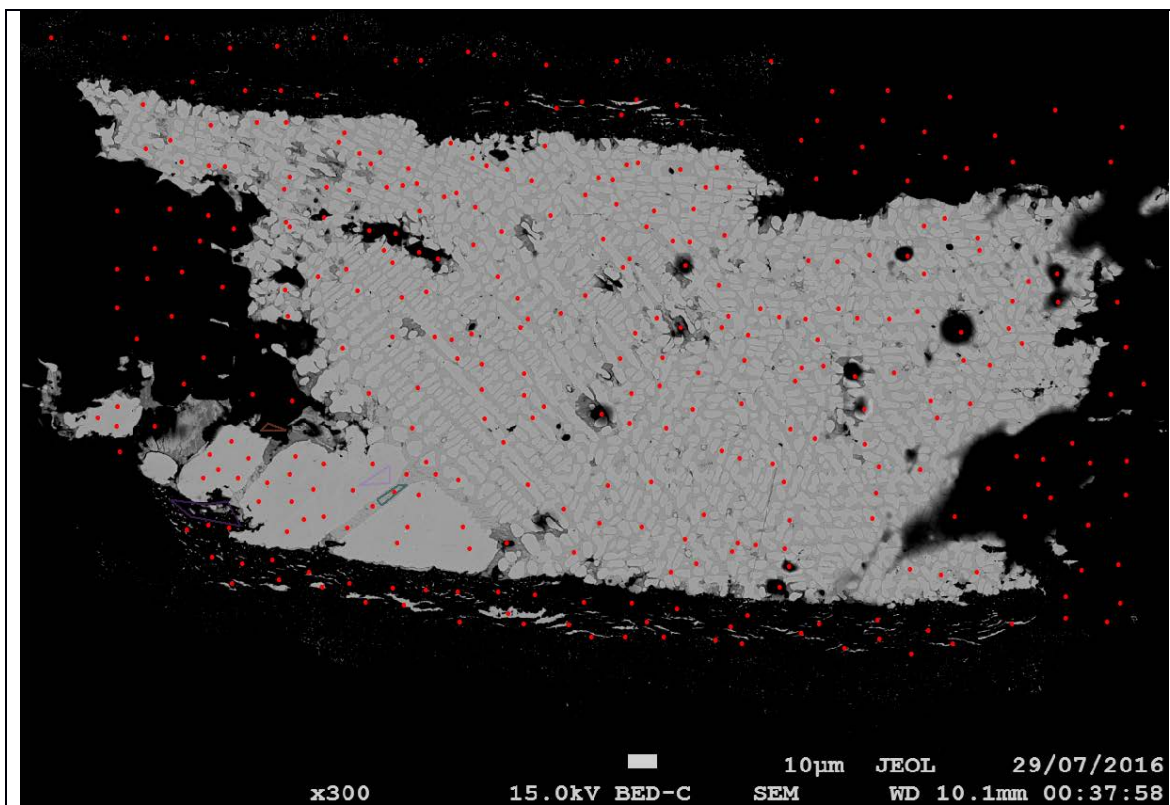
- Ritchie, N. W. (2013). Is Scanning Electron Microscopy/Energy Dispersive X-ray Spectrometry (SEM/EDS) Quantitative?. *Scanning*, 35(3), 141-168.
- Rivoldini, a., Van Hoolst, T., Verhoeven, O., Mocquet, a., & Dehant, V. (2011). Geodesy constraints on the interior structure and composition of Mars. *Icarus*, 213(2), 451–472.
- Robert, H. J., & Arkani-Hamed, J. (2014). Impact heating and coupled core cooling and mantle dynamics on Mars. *Journal of Geophysical Research: Planets*, 119, 729–744.
- Ruiz, J. (2014). The early heat loss evolution of Mars and their implications for internal and environmental history. *Scientific Reports*, 4(2), 4338.
- Sanloup, C., Guyot, F., Gillet, P., & Fei, Y. (2002). Physical properties of liquid Fe alloys at high pressure and their bearings on the nature of metallic planetary cores. *Journal of Geophysical Research: Solid Earth*, 107(B11).
- Sakai, T., Ohtani, E., Kamada, S., Terasaki, H. and Hirao, N., 2012. Compression of Fe88. 1Ni9. 1S2. 8 alloy up to the pressure of Earth's inner core. *Journal of Geophysical Research: Solid Earth*, 117(B2).
- Schubert, G., & Spohn, T. (1990). Thermal history of Mars and the sulfur content of its core. *Journal of Geophysical Research: Solid Earth*, 95(B9), 14095-14104.
- Shi, W. (2009). *Principles of modeling uncertainties in spatial data and spatial analyses*. CRC Press.
- Shomate, C. H. (1954). A Method for Evaluating and Correlating Thermodynamic Data. *The Journal of Physical Chemistry*, 58(4), 368-372.
- Sohl, F., & Spohn, T. (1997). The interior structure of Mars: Implications from SNC meteorites. *Journal of Geophysical Research: Planets*, 102(E1), 1613-1635.

- Stewart, A. J., Schmidt, M. W., Westrenen, W. Van, Liebske, C., & Wt, S. (2007). Mars: A New Core-Crystallization Regime.
- Stewart, A. J., van Westrenen, W., Schmidt, M. W., & Günther, D. (2009). Minor element partitioning between fcc Fe metal and Fe–S liquid at high pressure: The role of crystal lattice strain. *Earth and Planetary Science Letters*, 284(3), 302-309.
- Stevenson, D.J., Spohn, T. and Schubert, G., (1983). Magnetism and thermal evolution of the terrestrial planets. *Icarus*, 54(3), pp.466-489.
- Stevenson, D.J., (2001). Mars' core and magnetism. *Nature*, 412(6843), pp.214-219.
- Terasaki, H., Kamada, S., Sakai, T., Ohtani, E., Hirao, N., & Ohishi, Y. (2011). Liquidus and solidus temperatures of a Fe–O–S alloy up to the pressures of the outer core: Implication for the thermal structure of the Earth's core. *Earth and Planetary Science Letters*, 304(3), 559-564.
- Urakawa, S., Matsubara, R., Katsura, T., Watanabe, T. and Kikegawa, T., (2011). Stability and bulk modulus of Ni<sub>3</sub>S, a new nickel sulfur compound, and the melting relations of the system Ni–NiS up to 10 GPa. *American Mineralogist*, 96(4), pp.558-565.
- Urakawa, S., Someya, K., Terasaki, H., Katsura, T., Yokoshi, S., Funakoshi, K., ... Irifune, T. (2004). Phase relationships and equations of state for FeS at high pressures and temperatures and implications for the internal structure of Mars. *Physics of the Earth and Planetary Interiors*, 143-144, 469–479.
- Walder, P., & Pelton, A. D. (2005). Thermodynamic modeling of the Fe-S system. *Journal of phase equilibria and diffusion*, 26(1), 23-38.

- Wanke, H. and Dreibus, G., (1988). Chemical composition and accretion history of terrestrial planets. *Philosophical Transactions of the Royal Society of London A: Mathematical, Physical and Engineering Sciences*, 325(1587), pp.545-557.
- Williams, J. P., & Nimmo, F. (2004). Thermal evolution of the Martian core: Implications for an early dynamo. *Geology*, 32(2), 97-100.
- Williams, Q. (2009). Bottom-up versus top-down solidification of the cores of small solar system bodies: Constraints on paradoxical cores. *Earth and Planetary Science Letters*, 284(3), 564-569.
- Vilim, R., Stanley, S., & Hauck, S. A. (2010). Iron snow zones as a mechanism for generating Mercury's weak observed magnetic field. *Journal of Geophysical Research: Planets*, 115(E11).
- Yoder, C. F., Konopliv, A. S., Yuan, D. N., Standish, E. M., & Folkner, W. M. (2003). Fluid core size of Mars from detection of the solar tide. *Science*, 300(5617), 299-303.
- Zhan, X., & Schubert, G. (2012). Powering Ganymede's dynamo. *Journal of Geophysical Research: Planets*, 117(E8).
- Zhang, L., and Y. Fei, (2008). Effect of Ni on Fe-FeS phase relations at high pressure and high temperature, *Earth Planet. Sci. Lett.* 268, 212-218.

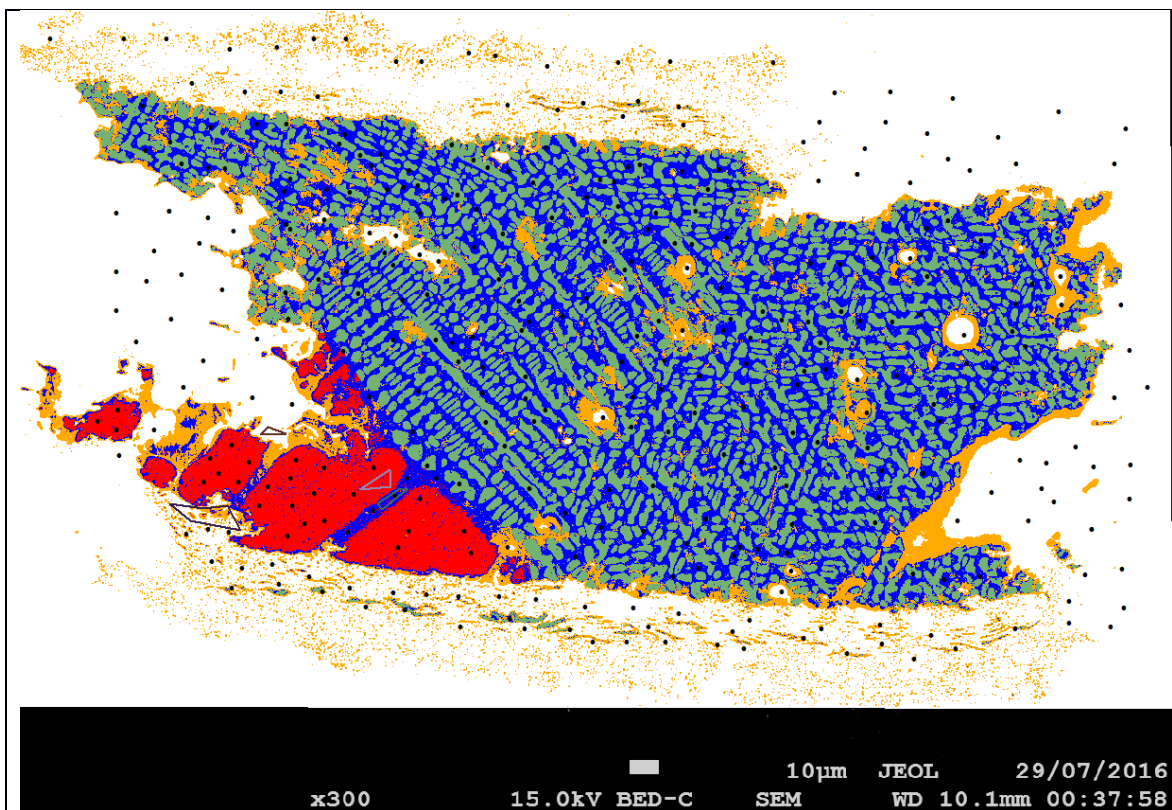
## Supplementary Tables &amp; Figures

Supplemental Table 1: Target S Composition Vs. Estimate							
FeS Grain Run ID	Target S (Wt. %)	Measured S (Wt. %)	Difference (Wt. %)	FeS Grain Run ID	Target S (Wt. %)	Measured S (Wt. %)	Difference (Wt. %)
M062916	1	0.56	0.44	M033116	1	2.39	1.39
M062816	3	11.99	8.99	M062516	1	1.43	0.43
M063016	3	12.19	9.19	M042216	2	1.3	-0.7
M020116	10	11.05	1.05	M040816	2	4.1	2.1
M021816	10	0.83	-9.17	M050116	2	2.7	0.7
M021116	10	0.7	-9.3	M050616	2	3.31	1.31
M022516	10	7.88	-2.12	M061516	2	5.63	3.63
M031916	10	0.85	-9.15	M061816	2	3.47	1.47
M090116	10	8.55	-1.45	M062616	2	2.88	0.88
				M050616	3	1.52	-1.48
				M052016	3	13.45	10.45
				M061116	5	9.6	4.6
				M053016	5	12.92	7.92
				M062016	5	0.19	4.71



**Supplemental Figure 1:** Point-based classification assessment of run M061816. Red dots are shape files generated across surface of the run. Green polygon is liquid training sample, pink polygon is droplet training sample, orange polygon is MgO training sample, and purple polygon represents both the solid and dendrite. Points are assigned a class identity based on the color of the raster beneath them, and are then converted to raster data.





**Supplemental Fig. 2:** Result of image classification. Green color is dendrite, blue is liquid, red is solid, orange is droplet, and MgO is white. The rasterized point's color has been made black to enhance clarity against classification colors. Once classification is performed, each point's identity assigned in the first step (Suppl. Fig. 1) is compared to what class it belongs to in the above image. The image's accuracy is the number of points that should have been assigned to a class divided by the amount that were actually assigned to that class (Shi, 2009).